

Slug bubble growth and dissolution by solute exchange

Daniël P. Faasen,^{*} Devaraj van der Meer,[†] Detlef Lohse,[‡] and Pablo Peñas[§]
*Physics of Fluids Group, Faculty of Science and Technology,
University of Twente, P.O. Box 217,
7500 AE Enschede, The Netherlands*

(Dated: November 18, 2021)

In many environmental and industrial applications, the mass transfer of gases in liquid solvents is a fundamental process during the generation of bubbles for specific purposes or, vice versa, the removal of entrapped bubbles. We address the growth dynamics of a trapped slug bubble in a vertical glass cylinder under a water barrier. In the studied process, the ambient air atmosphere is replaced by a CO₂ atmosphere at the same or higher pressure. The asymmetric exchange of the gaseous solutes between the CO₂-rich water barrier and the air-rich bubble always results in net bubble growth. We refer to this process as solute exchange. The dominant transport of CO₂ across the water barrier is driven by a combination of diffusion and convective dissolution. The experimental results are compared to and explained with a simple numerical model, with which the underlying mass transport processes are quantified. Analytical solutions that accurately predict the bubble growth dynamics are subsequently derived. The effect of convective dissolution across the water layer is treated as a reduction of the effective diffusion length, in accordance with the mass transfer scaling observed in laminar or natural convection. Finally, the binary water–bubble system is extended to a ternary water–bubble–alkane system. It is found that the alkane (n-hexadecane) layer bestows a buffering (hindering) effect on bubble growth and dissolution. The resulting growth dynamics and underlying fluxes are characterised theoretically.

I. INTRODUCTION

The dissolution of carbon dioxide gas and its subsequent transport through liquid layers plays an important role in many industrial and biological applications. Examples include enhanced oil recovery [1], CO₂ sequestration operations in porous media [2], and gas exchange in the respiratory system [3]. In microfluidics, segmented flows of alternating CO₂ gas and liquid plugs are frequently employed to study solvent absorption properties and chemical reaction kinetics [4–6]. In fact, the controlled dissolution of CO₂ bubbles constitutes a crucial step in the microfluidic generation of encapsulated microbubbles for ultrasound-imaging in medical diagnostics and targeted drug delivery [7, 8].

Bubble formation, however, can have detrimental effects on microfluidic devices such as blocking the liquid flow [9, 10]. Bubbles covering the electrode surface of electrochemical devices hinder gas-evolution reactions, thereby reducing the efficiency of the cell [11–15]. Similarly, bubble formation during inkjet printing can completely disrupt the printing process [16]. Therefore, thorough understanding of the solubility and transport of dissolved gas is clearly of benefit, not only upon encountering these complications, but also in an overwhelming number of applications concerning gas or vapor bubbles [17].

Multiple solutions for unwanted bubble removal exist, ranging from passive removal such as bubble traps, to active removal by increasing the driving pressure in order to increase the gas solubility and induce dissolution [9]. However, when performing the latter, one should take note of the gas composition inside the trapped bubble and surrounding liquid, as pressurising with a different gas species may very well cause the bubble to grow instead of dissolve.

This is precisely the focus of our work. We investigate the mass transfer experienced by a single slug air bubble trapped in a vertical glass cylinder beneath a thin layer of water which separates the bubble from the ambient gas, as shown in Fig. 1. We replace the ambient air atmosphere with a CO₂ atmosphere at the same or higher pressure, and study the subsequent growth dynamics of the bubble. Its growth is driven by the asymmetric exchange of gaseous solutes in the water layer (CO₂) with those in the trapped bubble (air). We therefore refer to this driving mechanism as solute exchange, where by replacing the gaseous solutes in a liquid solvent one is able to promote the growth (or dissolution) of the bubbles found therein. Solute exchange is fundamentally different from the solvent exchange mechanism used to generate microbubbles by replacing the liquid solvents [18, 19].

^{*} d.p.faaesen@utwente.nl

[†] d.vandermeer@utwente.nl

[‡] d.lohse@utwente.nl

[§] p.penaslopez@utwente.nl

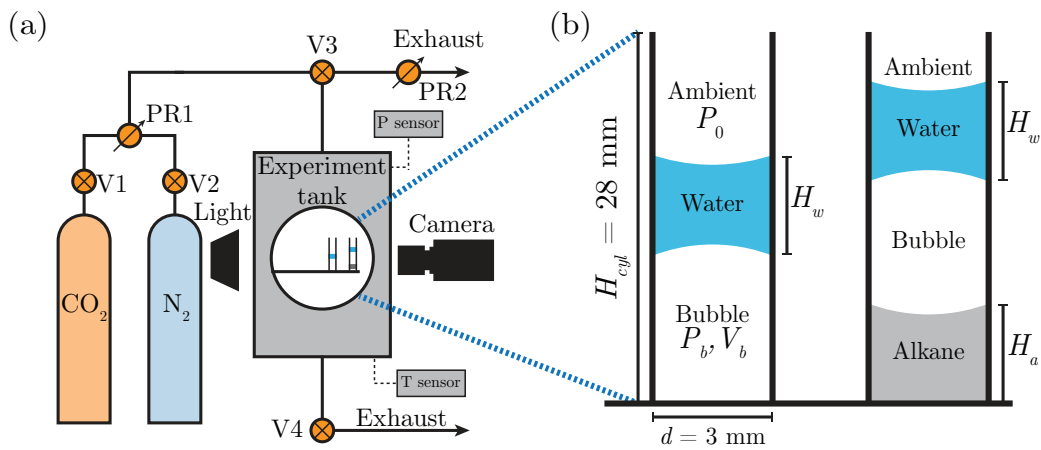


FIG. 1. (a) Schematic overview of the experimental set-up. (b) Sketch of the cylinders containing the water–bubble and water–bubble–alkane systems. These are placed inside the chamber, which is subsequently pressurised with CO₂ gas.

In a nutshell, our aim is to investigate the growth dynamics of a trapped slug bubble due to a solute exchange process induced by changes in the outer ambient gas composition. It will be seen that the bubble growth rate is in fact supradiffusive due to the onset of CO₂ dissolution-driven convection across the vertical water layer above the bubble. Convective dissolution or growth is indeed encountered in many relevant applications, such as CO₂ capture and storage in saline aquifers [2], buoyancy-generating chemical reactions [20, 21], droplet dissolution [22, 23] or bubble growth [24]. In essence, our system embodies a mass-transport variant of the classical problem of Rayleigh–Bénard convection [25] in a cylindrical cell. With this in mind, we devote significant effort to the quantification, both experimentally and theoretically, of the effect of convective dissolution on the bubble growth dynamics. Finally, the binary water–bubble system is extended to a ternary water–bubble–n-hexadecane system. Bubble growth dynamics will be seen to be hindered by the presence of the buffering alkane layer. Ternary configurations are of considerable relevance in gas–liquid–liquid three-phase microreactors [26]. The inclusion of oxygenated oil layers has also been shown to enhance bacterial growth in bioreactors [27], owing to the well-known fact that oils have higher gas solubilities than water [28–30].

This paper is structured as follows. The experimental set-up and procedure are described in section II. Section III offers a qualitative description of the solute exchange mechanism. Section IV presents quantitative results for the aforementioned binary water–bubble system. We propose a simple theoretical framework which adequately describes the bubble growth dynamics driven by (convection-enhanced) solute exchange. Experiments are compared to a numerical model and analytical solutions. The proposed dependence of the Sherwood number on the Rayleigh number across the water layer is compared to all binary and ternary experiments in section V. In section VI the ternary water–bubble–alkane system is investigated in greater detail, and the buffering effect of the n-hexadecane layer is characterised. The paper ends with a summary of the main findings and an outlook in section VII.

II. EXPERIMENTAL SET-UP AND PROCEDURE FOR SOLUTE EXCHANGE

A schematic overview of our experimental set-up is shown in Fig. 1(a). The experiments are conducted inside a sealed chamber which can be pressurised with either CO₂ or N₂ gas. The inlet pressure is adjusted using pressure regulator PR1, whereas a second pressure regulator, PR2, grants additional control of the ambient pressure P_0 inside the tank, where $1 \leq P_0 \leq 4$ bar. A temperature and a pressure sensor monitor the temperature T_0 and pressure P_0 in time. Extensive details on the chamber and pressure control system can be found elsewhere [31].

Two borosilicate glass (Duran) cylinders (28 mm in length, inner diameter $d = 3.0$ mm, outer diameter of 5.0 mm) are attached on one end to a silicon wafer plate using Loctite 4305 (Farnell), while the remaining end is left open. Before use, the cylinders are rinsed with ethanol (Boom, technical grade) followed by Milli-Q water (resistivity = 18.2 M $\Omega \cdot$ cm) and finally dried in a nitrogen stream.

The cylinders host either a water–bubble or a water–bubble–alkane configuration, as depicted in Fig. 1(b). The water–bubble system is prepared by injecting a slug bubble using an air-filled syringe between the plate wall and a previously deposited Milli-Q water layer of height $H_w = 2.5$ –6.0 mm. The bubble is held in place due to a stable balance between the weight of the water barrier and a combination of the surface tension of the water–bubble interface

and to a lesser extent the differences in gas pressures. This force balance persists during the experiments, given that the surface tension of CO_2 on water is almost the same as the surface tension of air on water under our experimental conditions [32]. For the water–bubble–alkane configuration, the bubble is similarly injected between a n-hexadecane layer (VWR, 99% purity) of height of $H_a \approx 3.0$ mm and the water layer, whose H_w was adequately chosen from within the same range of lengths as in the binary system for fair comparison. The selection of bubble volumes will be discussed shortly.

The experimental procedure is best illustrated with reference to a typical experiment shown in Fig. 2. The prepared cylinders are placed inside the experimental tank. The inlet pressure is set to 1.0 bar with valve V3 remaining closed. At time $t = 0$, the camera (Photron FASTCAM Nova s12, 2 fps) and the pressure/temperature sensors (2 acquisitions per second) start recording. At this point, the water–bubble and water–bubble–alkane systems will be in the equilibrium state [Fig. 2(a)]. The volume of any particular bubble, $V_b(t)$, is initially at equilibrium: $V_b(0) \equiv V_{eq}$. At time $t_{f-start} = 5$ s, valves V3 and V4 [see Fig. 1(a)] are opened and the system is flushed with CO_2 gas in order to fully replace the ambient air in the experimental chamber. This corresponds to the “flush” stage in Fig. 2(e), which plots the pressure inside the experimental chamber, $P_0(t)$, during the initial minutes of that particular experiment. After flushing for 60 seconds, valve V4 is closed and P_0 is set to the pressure level of the “experiment” stage, e.g., $P_0 = 2.0$ bar for the experiment in Fig. 2. The time t_f [typically 75 s, see Fig. 2(e)] importantly refers to the time immediately after the flushing and compression stages have been completed and marks the start of the “experiment” stage. The bubble volume at this point [cf. Fig. 2(b)] is coherently denoted by $V_f \equiv V_b(t_f)$. Thereafter, despite pressurization, both bubbles experience continuous growth – counterintuitive perhaps – as a consequence of solute exchange. The growth is showcased by snapshots in Fig. 2(b–d) and its dynamics is quantified in the $V_b(t)$ plot in Fig. 2(f). At the end of the experiment (one hour in this case), valves V1–V3 are closed and V4 is opened in order to depressurise the system. The bubble volumes are extracted from the images using an in-house developed Matlab script.

Several experiments similar to the one just described were performed for binary and ternary systems, or a combination thereof, comprising either a single-system (one-cylinder) experiment or a two-system (two-cylinder) experiment like the one shown in Fig. 2. The pressure level $P_0(t > t_f)$ ranged from 1 bar (no compression after flushing) up to 4 bar, with running times of typically one or two hours. The initial bubble volumes considered correspond to (post-pressurization) volumes of $25 \mu\text{L} < V_f < 45 \mu\text{L}$ (3.5 to 6.4 mm in height). The ambient temperature remained fairly constant at approximately $T_0 = 295$ K for every experiment.

It should be stressed that when pressurising the chamber above the atmospheric pressure [$P_0(t > t_f) > 1.0$ bar], the bubble volume compresses from V_{eq} to V_f accordingly [cf. Fig. 2(a, b)], as established by Boyle’s law. Moreover, the movement of the contact lines during compression also alters the shape of the bubble menisci, which may even take an additional few seconds to reform and settle. In some cases, we were unable to capture V_{eq} with sufficient accuracy due to optical limitations. For these reasons, the reference bubble volume is taken to be V_f instead of V_{eq} . This decision is justified provided that any changes in the molar gas contents in the bubble (initially air) remain negligible during $t < t_f$, i.e., under the assumption that there is insignificant mass transfer to or from the bubble up to that point. The experiments conducted at $P_0(t > t_f) = 1.0$ bar (devoid of pressurisation) fully support the above assumption: V_f was seen to effectively remain unchanged from V_{eq} .

III. SOLUTE EXCHANGE MECHANISM

The replacement of the air atmosphere inside the experimental chamber by CO_2 gas causes the latter to dissolve into the water layer, where a CO_2 -concentration boundary layer naturally develops. Hence, CO_2 is transported down towards the water–bubble interface, where it exsolves into the bubble. The steady-state diffusive influx into the bubble (in the absence of convection) can be estimated noting that the concentration of dissolved CO_2 at the water–bubble interface is initially close to zero, whereas at the water–ambient interface it is $S_{\text{CO}_2}^w P_0$, where $S_{\text{CO}_2}^w$ denotes the Henry coefficient of CO_2 in water. The flux estimate is therefore $S_{\text{CO}_2}^w P_0 / H_w$, where H_w is the height of the water column, see Fig. 1.

At the same time, an air concentration gradient forms across the water layer, sustaining a diffusive flux in the opposite direction, i.e., from the (air-rich) bubble to the (air-depleted) CO_2 atmosphere. The corresponding diffusive outflux can be estimated in the same manner as $S_{air}^w P_0 / H_w$, where S_{air}^w denotes the molar-averaged Henry coefficient of the air mixture in water. The high solubility of CO_2 in water (cf. the solubilities listed in Table I) implies that the CO_2 influx is stronger than the air outflux by a factor of $S_{\text{CO}_2}^w / S_{air}^w \approx 42$. This clear disparity in the magnitude between both solute exchange fluxes results in net bubble growth as seen in Fig. 2.

The time required for diffusion to develop a linear CO_2 -concentration profile across the full height of the water layer can be estimated as $\sim 0.4 H_w^2 / D_{\text{CO}_2}^w$ from simple theoretical considerations [see appendix A, Fig. 10(a)], where $D_{\text{CO}_2}^w$ denotes the diffusivity of CO_2 in water. For the experiment portrayed in Fig. 2 where $H_w = 3$ mm, the bubbles would

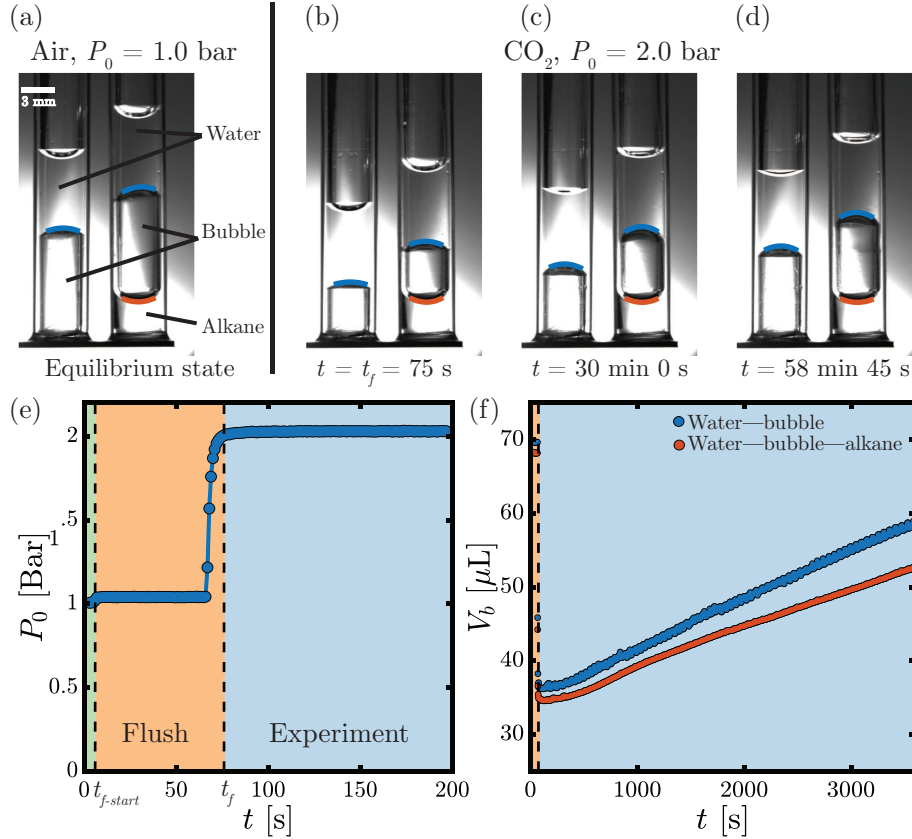


FIG. 2. A typical experiment involving a binary and ternary system. Experimental snapshots at (a) $t = 0$, equilibrium state, (b) $t = t_f$, immediately after CO_2 -flushing and pressurisation, (c) halfway through the experiment and (d) at the end of the experiment. The blue line indicates the bubble–water interface detected by the contour detection algorithm. Similarly, in the right cylinder with the alkane, the red line indicates the detected bubble–alkane interface. (e) Time evolution of the pressure in the tank during the first 200 seconds of the experiment. Before $t_{f\text{-start}}$ (green stage) the tank is filled with ambient air. Between $t_{f\text{-start}}$ and t_f (orange stage) the tank is flushed with CO_2 and the bubbles are compressed. (f) Evolution in time of the bubble volume for the two systems.

require an initial transient period of $\sim 2,000$ s before the maximum quasi-steady growth rate is attained. However, Fig. 2(f) clearly shows that the transient period is substantially smaller, of approximately 300 s. Thus, without further calculation, it is evident that convective dissolution must have a dominant influence on the bubble growth. Its effect will be unraveled next in Sec. IV.

Finally, Fig. 2(f) also reveals that the presence of the n-hexadecane layer slows down bubble growth. Essentially, part of the CO_2 accumulating into the bubble is redissolving into the hexadecane layer, given that it is initially depleted of CO_2 . The stabilising or buffering effect of the alkane layer on the bubble growth (and dissolution) dynamics will be discussed in detail in Sec. VI.

TABLE I. Henry’s constants and diffusion coefficients of the gases in water (superscript w) and n-hexadecane (superscript a) at 293.0 K and 1.0 bar. The molar-averaged S_{air}^w can be estimated as $9.02 \times 10^{-6} \text{ mol/m}^3 \text{ Pa}$.

| j | S_j^w [mol/m ³ Pa] | S_j^a [mol/m ³ Pa] | D_j^w [m ² /s] | D_j^a [m ² /s] |
|---------------|---------------------------------|---------------------------------|-----------------------------|---|
| CO_2 | 3.79×10^{-4} [28] | 4.06×10^{-4} [29] | 1.76×10^{-9} [33] | 2.20×10^{-9} [34] |
| O_2 | 1.32×10^{-5} [28] | 6.45×10^{-5} [30] | 2.03×10^{-9} [35] | 2.49×10^{-9} ^a [36] |
| N_2 | 6.89×10^{-6} [28] | 4.61×10^{-5} [30] | 2.00×10^{-9} [37] | 2.49×10^{-9} ^b |

^a Only available at 294.0 K.

^b Approximated value based on the diffusion coefficient of oxygen in n-hexadecane.

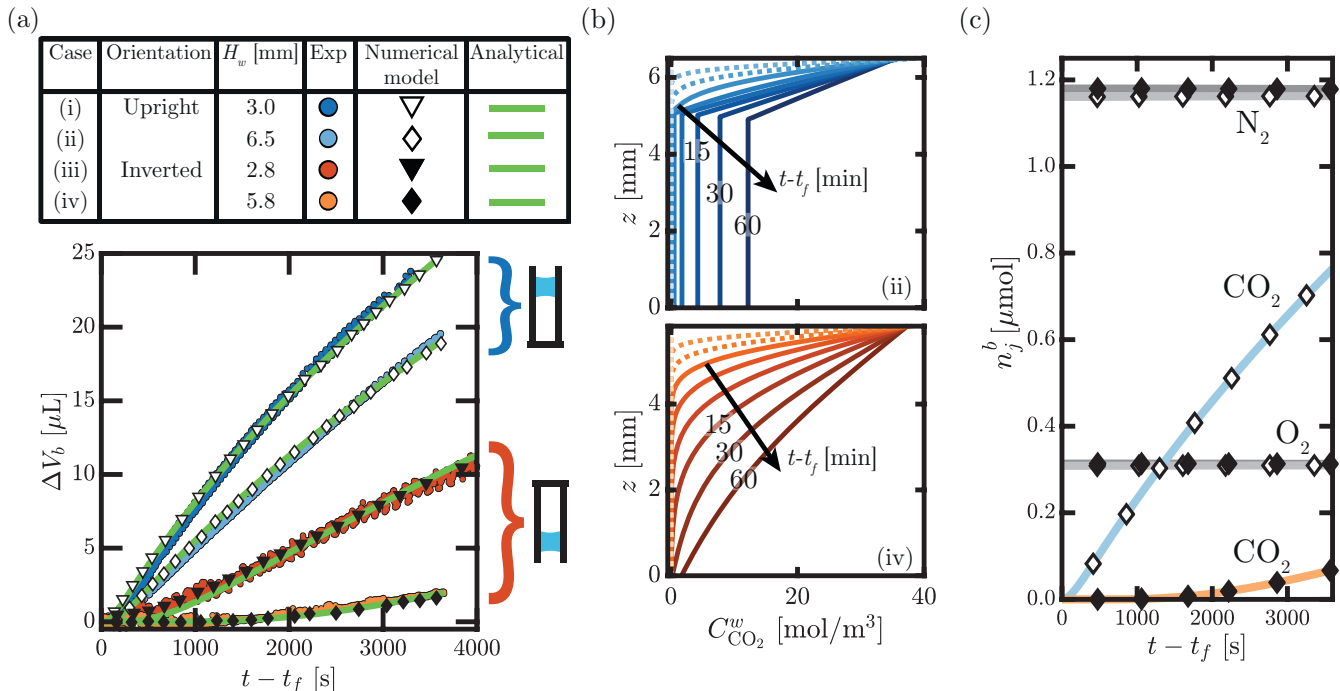


FIG. 3. Experimental and theoretical results for water–bubble systems in an upright configuration (cases i, ii) and inverted configuration (cases iii, iv) for two distinct water layer heights; the experiment pressure level is $P_0(t > t_f) = 1$ bar and bubble volumes are initially $V_f = 35 \mu\text{L}$. (a) Bubble growth dynamics ($\Delta V_b \equiv V_b(t) - V_f$), according to experiment (circles), numerical model (black/white markers) and analytical solutions (green lines); the latter are given by (13) for (iii, iv) and (17) for (i, ii). The onset of convective dissolution for upright cases (i, ii) is evident. (b) Time evolution of the CO_2 concentration profiles in the water layer according to the model for convective dissolution case (ii) and pure diffusion case (iv). The uniform profile outside the diffusion boundary layer in case (ii) illustrates the model assumption of instant convective transport. (c) Time evolution of the gas composition in the bubble according to the model for upright case (ii) [white markers and lighter curves], and inverted case (iv) [black markers and darker curves].

IV. SOLUTE EXCHANGE IN THE WATER–BUBBLE SYSTEM

In this section, we focus solely on the experiments concerning the binary (bubble–water) configuration. We present a theoretical framework for diffusion-driven solute exchange with the additional effect of dissolution-driven convection. The insight gained from a simple numerical model allows us to derive analytical solutions that accurately describe the dynamics of bubble growth.

A. Effect of convective dissolution

We begin analysing a series of single-cylinder, water–bubble experiments concerning a bubble of equilibrium volume $V_{eq} = 35 \mu\text{L}$ capped by a water layer with a thickness of either $H_w \approx 3$ mm or $H_w \approx 6$ mm. The prepared cylinders were placed in the experimental chamber, positioned either upright or inverted (rotated 180°), as illustrated in Fig. 3(a). Subsequently, the air inside the chamber was replaced by a CO_2 atmosphere at $P_0(t > t_f) = 1$ bar. Therefore, the bubble volume at the start of the “experiment” stage, $V_f \equiv V_b(t_f)$, is equal to V_{eq} .

The increase in bubble volume with time, $\Delta V_b(t) \equiv V_b(t) - V_f$, is shown for both the upright cases (i, ii) and inverted cases (iii, iv) in Fig. 3(a). The bubbles in the upright configuration are seen to grow much faster than when inverted under otherwise the same conditions. As a consequence, this difference should be attributed to the effect of convective dissolution. In the upright cases, the dense CO_2 -rich boundary layer that forms at the top of the water phase becomes gravitationally unstable. This gives rise to dissolution-driven convection in the form of CO_2 -rich viscous fingers or plumes that propagate downwards at relatively high speeds [2, 38–41]. In contrast, the CO_2 -water mixture is stably stratified when the cylinder is placed inverted and therefore CO_2 can only be transported up the water layer by diffusion.

In the absence of convection, the diffusive transport of the solute exchange (and consequently the bubble growth dynamics) is governed by the one-dimensional diffusion equation for the molar concentration,

$$\frac{\partial C_j^w}{\partial t} = D_j^w \frac{\partial^2 C_j^w}{\partial z^2}, \quad (1)$$

across the water layer ($0 < z < H_w$) for three gas species: $j = \text{CO}_2$, $j = \text{O}_2$, and $j = \text{N}_2$, where the latter two represent the air mixture. In doing so, we neglect the three-dimensional curvature of the bubble meniscus, whose height is indeed small in comparison with H_w [cf. Fig. 2(a–d)]. The diffusivity of gas j in water is denoted by D_j^w . The diffusive fluxes across the water–bubble interface on $z = 0$ are therefore $J_j^{wb} = -D_j^w \partial_z C_j^w(0, t)$. The ambient pressure $P_0(t)$ and the partial pressures in the ambient are prescribed at all times, and these can be interpolated and inferred from the experimental pressure data. The pressure inside the bubble $P_b(t)$ is assumed equal to $P_0(t)$ at all times, given that the capillary overpressure in the bubble is negligible: $4\sigma/d \ll P_0$, with σ as the surface tension. The partial gas pressures in the ambient and the bubble set the interfacial concentrations (boundary conditions) of Eq. (1) as established by Henry’s law (see appendix B). The bubble contents are treated as a mixture of ideal gases, whence $P_0 V_0 = n_b R T_0$, where R is the universal gas constant and $n_b = n_{\text{CO}_2}^b + n_{\text{N}_2}^b + n_{\text{O}_2}^b$ the number of moles of gas in the bubble (neglecting other gases which are present in small amounts ($< 1\%$)). Finally mass conservation, $J_j^{wb} \pi d^2 / 4 = \dot{n}_j^b$, yields the volume growth rate:

$$\dot{V}_b = \frac{\pi d^2}{4} \frac{R T_0}{P_0} \sum_j J_j^{wb}. \quad (2)$$

The above system (1)–(2) is solved and integrated numerically by means of a finite-differences scheme. A complete description of the model equations, initial conditions and numerical implementation can be found in appendix A. The resulting time evolution $V_b(t)$ is plotted by the black markers in Fig. 3(a) for cases (iii) and (iv). Good agreement is found between these and experiments.

It should be pointed out that we neglect the influence of water vapor (evaporation) on the bubble growth, despite the likely fact that the bubble is saturated with water vapor. This is justified since the water vapour pressure is small, $P_w^{sat}/P_0 < 2\%$ and its inclusion in the theoretical framework would add little insight at the cost of added complexity. Water evaporation, unlike solute exchange, is not a driving force for bubble growth. Instead, the role of evaporation is merely to ensure that the bubble remains saturated with water vapour at all times. It can be shown that evaporation fluxes amplify $\dot{V}_b(t)$ by a factor $(1 - P_w^{sat}/P_0)^{-1}$; the resulting difference still remains within the experimental uncertainty of V_b .

Next, we incorporate the effect of convective dissolution into the solute exchange diffusive framework established so far. Convective transport of CO_2 across the water layer is characterised by the instantaneous Rayleigh and Sherwood numbers,

$$Ra_w(t) \equiv \frac{\lambda_{\text{CO}_2}^w \Delta C_{\text{CO}_2}^w(t) g H_w^3}{\nu_w D_{\text{CO}_2}^w}, \quad Sh_w(t) \equiv \frac{J_{\text{CO}_2}^{wb}(t) H_w}{D_{\text{CO}_2}^w \Delta C_{\text{CO}_2}^w(t)}, \quad (3)$$

where g is the acceleration due to gravity, ν_w the kinematic viscosity of water and $\lambda_{\text{CO}_2}^w \approx 8.2 \text{ cm}^3/\text{mol}$ the solutal expansion coefficient of CO_2 in water at $T_0 = 295 \text{ K}$ [42, 43]. The instantaneous concentration difference across the water layer is established by the partial pressure difference of CO_2 gas that exists between the ambient and the bubble: $\Delta C_{\text{CO}_2}^w(t) = S_{\text{CO}_2}^w [P_{\text{CO}_2}^0(t) - P_{\text{CO}_2}^b(t)]$.

In view of the modest aspect ratios of the water column considered in our experiments ($0.45 < d/H_w < 1.3$), we have adopted H_w as the relevant length scale, in agreement with the classical definition of the Rayleigh number in the field of Rayleigh–Bénard convection [44, 45]. Here it is worth noting that in contrast to the above choice, convective dissolution studies often employ porous Rayleigh and Sherwood numbers based on the permeability of the porous medium [2, 38, 40, 46]. There, the permeability scales as d^2 , namely, the square of the highly restrictive pore size or the Hele-Shaw cell thickness.

The characteristic Rayleigh number can be readily estimated from Eq. (3) inserting $H_w = 3.0 \text{ mm}$, $P_{\text{CO}_2}^0 - P_{\text{CO}_2}^b = 1.0 \text{ bar}$ in addition to the diffusivities and solubilities tabulated in Table I. We obtain $Ra_w \approx 3 \times 10^4$, which is well above the critical value, $Ra_c = 1708$, for the onset of convection in an infinitely wide enclosure ($d/H_w \rightarrow \infty$) [45, 47]. The Schmidt number is large: $Sc = \nu_w/D_{\text{CO}_2}^w = 568$. Therefore, our moderate- Ra_w , high- Sc experiments should lie in the viscosity-dominated regime (also large-Prandtl or laminar regime [45], or regime I_u in the Grossmann–Lohse theory [44]), where buoyancy forces are indeed balanced by viscous forces. We therefore expect a $Sh_w \sim Ra_w^{1/4}$ dependence [44, 45], consistent with measurements of laminar Rayleigh–Bénard convection [48], and natural convection adjacent

to horizontal surfaces [49, 50], dissolving drops [22, 23] or growing bubbles [24]. This laminar regime should not be mistaken with that of viscous convection of an infinite-Prandtl or Schmidt fluid in the limit of large Rayleigh numbers. For such a case, the scaling $Sh_w \sim Ra_w^{1/5}$ is expected between (no-slip) solid surfaces [51, 52] (cf. regime I_∞ of the G–L theory [53]) and $Sh_w \sim Ra_w^{1/3}$ between (zero shear stress) free surfaces [51, 52, 54]. However, the robustness of the 1/4 exponent present in all the aforementioned cases of laminar convection hints that neither the no-shear boundary condition nor the cell geometry impact the scaling significantly. In our case, this is further justified by noting that the aspect ratio remains always close to unity, and the fact that bubble surfaces are prone to contamination by impurities naturally present in the ambient and can consequently behave as no-slip [55]. Nevertheless, the prescribed scaling $Sh_w \sim Ra_w^{1/4}$ will be verified experimentally later in section V.

Provided that variations in $Ra_w(t)$ are sufficiently slow, we assume that the dependance of the quasi-steady Sherwood number on the instantaneous Rayleigh number is of the form

$$Sh_w(t) = \left[1 + k \frac{Ra_w(t)}{Ra_c} \right]^{1/4}, \quad (4)$$

where $Ra_c = 1,708$ and $k = 2.75 \pm 1.25$ is a dimensionless fitting coefficient that can be systematically obtained from the experimental measurements, as will be shown later in section V. The fitting coefficient k is expected to depend on Sc and the aspect ratio d/H_w of the system but otherwise it is ideally a constant. Its variability across the experiments arises from several factors such as the different aspect ratios employed, uneven shapes of the bubble menisci, or the heterogeneous wetting state of the cylinder walls. In short, part of the variability is bound to the experimental uncertainty involving $V_b(t)$. Furthermore, the requirement that (4) should well capture the transition from pure diffusive transport ($Sh_w = 1$ for $Ra_w < Ra_c$) to convection-dominated transport ($Sh_w \sim Ra_w^{1/4}$ for $Ra_w \gg Ra_c$) is not at all important here, since all of our experiments correspond exclusively to the latter. To model details of the transition, an additional fitting parameter could be employed cf. Ref. [22].

At this point, we must invoke additional physical assumptions inspired by Howard’s [56] and Malkus’ [57] phenomenological treatment of turbulent Rayleigh–Bénard convection. Firstly, we assume that most of the concentration drop $\Delta C_{CO_2}^w$ occurs across the top diffusive boundary layer, whereas the convective region in the bulk of the water layer acts as a short-circuit for mass transfer. The concentration drop across the bottom boundary layer is assumed to be negligible. This structure is sketched in Fig. 4(a). Secondly, we assume that the top boundary layer must always be in a ‘marginally stable state’ once it develops. This means that boundary layer cannot surpass (or shrink below) a critical or stable size $\delta(Ra_w)$ which is such as to ensure that the quasi-steady mass transfer rate across the water layer is precisely given by (4). Note that the thickness of the concentration boundary layer is connected to Sh_w by $\delta \sim H_w/Sh_w$ [44, 45], hence, we see that $\delta/H_w \sim Ra_w^{-1/4}$.

Under these circumstances, the quasi-steady (fully developed) concentration profile across δ can be considered linear. The quasi-steady flux is thus $J_{CO_2}^{wb} = D_{CO_2}^w \Delta C_{CO_2}^w / \delta$. Inserting this result into the definition of Sh_w in (3), we determine the stable quasi-stationary thickness of the boundary layer to be

$$\delta(t) = \frac{H_w}{Sh_w(t)} = H_w \left[1 + k \frac{Ra_w(t)}{Ra_c} \right]^{-1/4}. \quad (5)$$

Therefore, we ultimately treat convection as the shortening of the effective diffusion layer from H_w to $\delta(t)$, as illustrated in Fig. 4(b). This treatment could be applied in the modelling of the various different regimes in the Sc , Ra_w parameter space [44] or even to situations where forced convection plays a role, in which case the governing relation in Eq. 4 should be adapted accordingly. In our numerical model, we simply solve the diffusion equation for $C_{CO_2}^w$ over the domain $0 < z < \delta(t)$, where $\delta(t)$ is reevaluated at every time step. The resulting numerical growth curves are plotted with white markers in Fig. 3(a) for cases (i) and (ii), with good general agreement. Eq. (5) also explains why the bubble growth rate still decreases with H_w despite the fact that $Ra_w \propto H_w^3$. Indeed, it follows that $\delta \propto H_w^{1/4}$, and a longer diffusion distance translates into weaker fluxes and slower growth.

The good performance of the model extends to experiments at higher pressures, as shown in Fig. 5(a). Here, the growth rate of bubbles with post-pressurization volumes $V_f = 35 \mu\text{L}$ under a water layer of $H_w \approx 4.5 \text{ mm}$ are compared for pressure levels $P_0(t > t_f) = 1.0, 2.0$ and 3.1 bar . It becomes clear that \dot{V}_b increases with pressure level P_0 . This result, perhaps counterintuitive, is purely a consequence of the stronger convection, since $Ra_w \propto (P_0 - P_{CO_2}^b) \sim P_0$. Note that in the absence of convection (pure diffusion), \dot{V}_b remains fairly independent of P_0 , since both the diffusive CO_2 fluxes and the CO_2 density in the bubble are proportional to P_0 .

The validity of the quasi-steady approximation of $Sh_w(t)$ and $\delta(t)$ implied by the model in Eq. (5) can be assessed from the time evolution of $\delta(t)$ and $Ra_w(t)$ for any particular experiment. We select the $P_0(t > t_f) = 3.1 \text{ bar}$ experiment from Fig. 5(a) for this matter; the results are shown in Fig. 5(b). Before flushing and the onset of

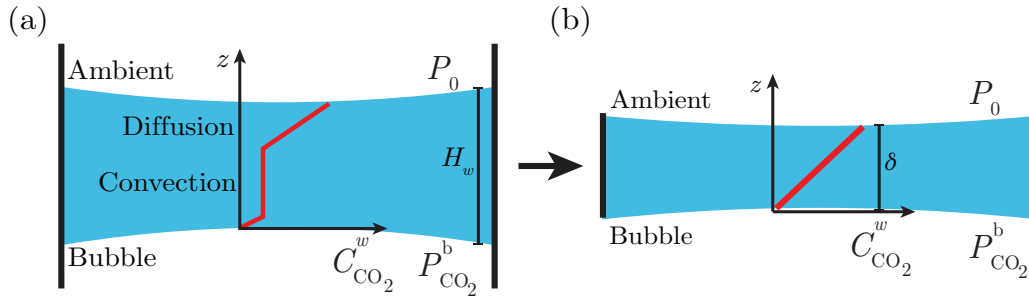


FIG. 4. (a) Sketch of the quasi-steady concentration profile of CO_2 across the water layer after the onset of convective dissolution. The main concentration drop occurs across the top diffusion boundary layer. Transport through the convective layer is assumed instant. The concentration drop across the bottom boundary layer is neglected. This is equivalent to (b), where the water layer is treated as a single diffusion layer of thickness $\delta(t) \sim H_w Ra_w(t)^{-1/4}$, where $Ra_w(t) \propto [P_0 - P_{\text{CO}_2}^b(t)]$, the difference in the partial pressure of CO_2 in the CO_2 -ambient and the bubble.

convection, $\delta/H_w = 1$. At the start of the flushing stage, at $t = t_{f\text{-start}}$, the critical size for stability shrinks to $\delta/H_w \approx 0.22$ in accordance to Eq. (5), i.e., as established by the instantaneous $Ra_w(t)$ at the flushing pressure of approximately 1 bar. Upon compression to $P_0 = 3.1$ bar shortly before t_f , $\delta(t)$ shrinks further accordingly. Thereafter, bubble growth and the concomitant increase in $P_{\text{CO}_2}^b(t)$ causes $\delta(t)$ and $Ra_w(t)$ to slowly increase and decay, respectively. The slow $\delta(t > t_f)$ dynamics supports the quasi-steady approximation.

The simplicity of this approach imposes no restriction to the initial diffusive development of the boundary layer in the model. We illustrate this in Fig. 5(b) by plotting the time evolution of δ_{99} , the distance over which 99% of the concentration drop takes place. As soon as flushing begins at $t_{f\text{-start}}$, we assume that the ambient air in the tank is instantaneously replaced by CO_2 , which sets the top boundary condition to $C_{\text{CO}_2}^w(H_w, t) = S_{\text{CO}_2}^w P_0(t_{f\text{-start}})$. The boundary layer evolves in a self-similar manner, and the concentration profiles can be well described by the self-similar solution

$$C_{\text{CO}_2}^w(z, t) = S_{\text{CO}_2}^w P_0(t_{f\text{-start}}) \operatorname{erfc} \left(\frac{H_w - z}{\sqrt{4D_{\text{CO}_2}^w(t - t_{f\text{-start}})}} \right). \quad (6)$$

The diffusive boundary layer $\delta_{99}(t)$ eventually attains the critical size δ , after which $\delta_{99} = \delta$ and across it a linear concentration profile develops. Pressurization at t_f would of course alter the self-similar development of the profiles in the strictest sense. Nonetheless, we see that the saturation time of δ_{99} is short – most of the δ_{99} development occurs within the short timeframe of the flushing stage itself. In fact, this saturation time, namely, the time required for the self-similar regime to transition towards the δ -bounded, quasi-steady regime, can be estimated as $0.3\delta_f^2/D_{\text{CO}_2}^w$, where $\delta_f \equiv \delta(t_f)$ is the effective diffusion length (see appendix A, Fig. 10). The concentration profiles for a previous experiment (where $P_0(t > t_f) = 1$ bar) drawn in Fig. 3(b) clearly demonstrate the rapid initial development of the boundary layer in convective experiments. On the other hand, for diffusive experiments [see profiles in Fig. 3(b)], the boundary layer saturation time is $0.3H_w^2/D_{\text{CO}_2}^w$, i.e., an order of magnitude larger, which results in a noticeably longer initial transient period of slow bubble growth.

Finally, we turn our attention to the gas composition of the bubbles over time, see Fig. 3(c). The air (O_2 and N_2 gas) content in the growing bubbles appears to remain virtually unchanged throughout the duration of the experiments by virtue of the low solubility of air in water. This observation is especially true for the bubbles growing at $P_0(t > t_f) = 1$ bar – Fig. 3(c) precisely – since the concomitant air fluxes are weakest then. Therefore, to a good approximation, the growth in bubble volume can be fully attributed to the uptake of CO_2 from the water layer. This result is pivotal in the derivation of the analytical solutions for bubble growth presented in the next subsection.

B. Analytical solutions for bubble growth

In the analysis that follows, we consider the bubble volume dynamics for $t > t_f$, i.e., after flushing and pressurization. The initial bubble volume is thus $V_b(t_f) \equiv V_f$. We denote the experiment pressure level $P_0(t > t_f)$ simply as P_0 , which is treated as constant in all regards. It follows that the partial pressure of CO_2 in the ambient is $P_{\text{CO}_2}^0(t > t_f) = P_0$ precisely. Furthermore, we assume that the flushing and pressurisation stage takes place instantaneously at t_f ,

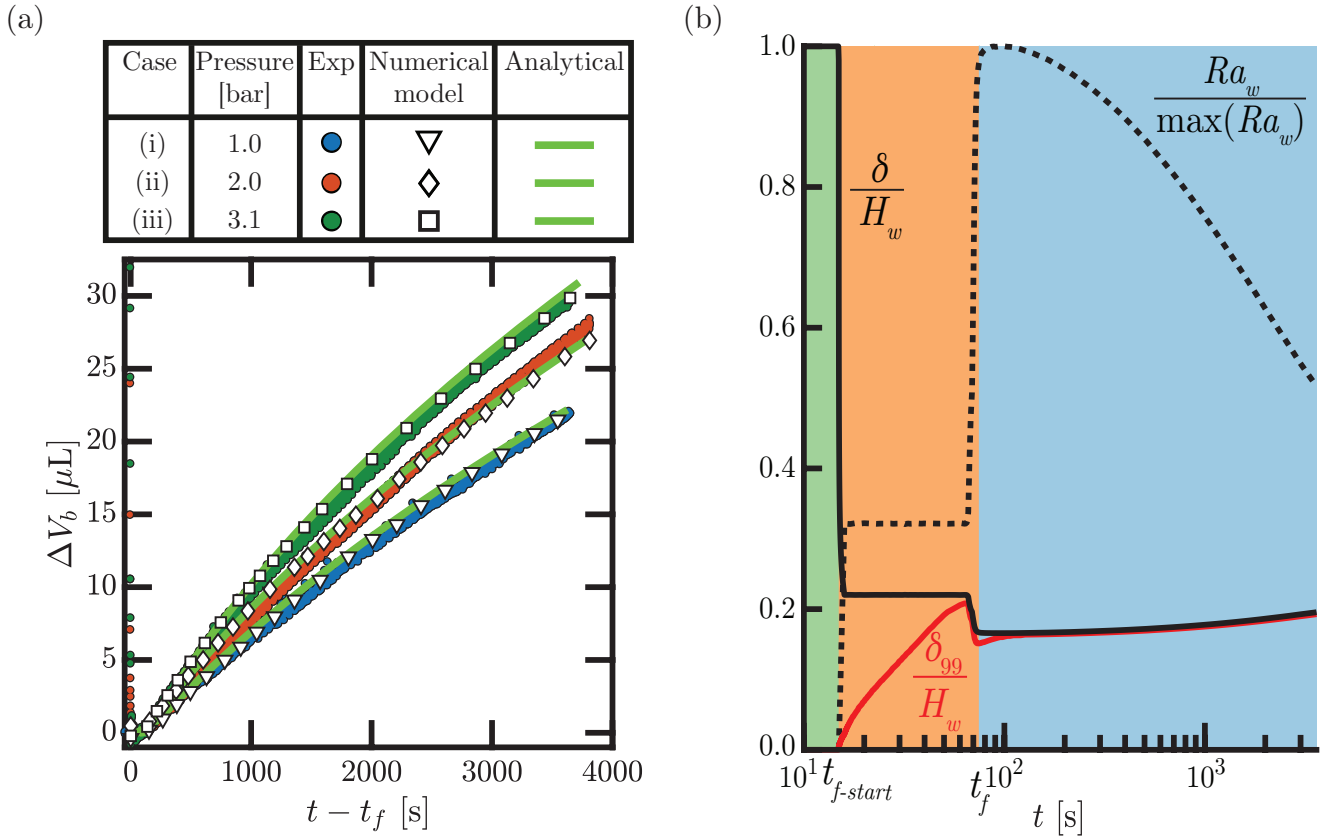


FIG. 5. (a) Effect of increasing the experiment pressure level $P_0(t > t_f)$ on the bubble growth dynamics. Water layer height is $H_w \approx 4.5$ mm and post-pressurization volumes are $V_f \approx 35$ μL . Experimental, numerical and analytical – Eq. (17) – results are compared. (b) Time evolution of the boundary layer thickness for marginal stability, $\delta(t)$ (black solid line), as established by its concomitant Rayleigh number (dotted line) according to the numerical model for experiment (iii) where $P_0(t > t_f) = 3.1$ bar. The red solid line represents δ_{99} , the distance over which 99 % of the numerical concentration drop takes place. Equilibrium, flushing and experiment stages are shaded accordingly (see Fig. 2).

meaning that at $t < t_f$ we consider equilibrium conditions everywhere in the system. This is reasonable since the flushing period ($t_f - t_{f-start}$) typically lasts 60 s, i.e., it is quite short in comparison to the relevant characteristic diffusion times.

Finally, we treat air as insoluble, i.e., we neglect the flux of O_2 or N_2 across the bubble or water layer. The number of moles of gas in the bubble can be then decomposed as

$$n_b(t) = n_{\text{CO}_2}^b(t) + n_{\text{N}_2}^b(t_f) + n_{\text{O}_2}^b(t_f), \quad (7)$$

with, initially, $n_{\text{CO}_2}^b(t_f) = 0$. We can then transform the above equation into a pressure–volume relationship. To do so, we make use of the ideal gas law, $P_0 V_b = n_b R T_0$ and the definition of the partial pressure of CO_2 in the bubble, $P_{\text{CO}_2}^b = n_{\text{CO}_2}^b P_0 / n_b$. Noting that $P_0 V_f = n_b(t_f) R T_0$ initially, we obtain the following relationship:

$$1 - \frac{P_{\text{CO}_2}^b(t)}{P_0} = \frac{V_f}{V_b(t)}. \quad (8)$$

Next, recalling the definition of Sh_w (Eq. (3)), we find it useful to non-dimensionalize the net molar flux into the bubble, $\dot{n}_b / (\pi d^2 / 4)$, in the same manner. We refer to it as the dimensionless bubble growth rate:

$$\phi_b(t) \equiv \frac{\dot{n}_b(t)}{\pi d^2 / 4} \frac{H_w}{D_{\text{CO}_2}^w \Delta C_{\text{CO}_2}^w(t)}. \quad (9)$$

Substituting in the ideal gas law $\dot{n}_b = P_0 \dot{V}_b / RT_0$, using Henry's law $\Delta C_{\text{CO}_2}^w(t) = S_{\text{CO}_2}^w [P_0 - P_{\text{CO}_2}^b(t)]$ and relationship (8), Eq. (9) becomes

$$\phi_b(t) = \frac{\dot{V}_b(t) V_b(t)}{Q V_f}, \quad \text{where} \quad Q \equiv D_{\text{CO}_2}^w \frac{\pi d^2}{4H_w} (S_{\text{CO}_2}^w RT_0). \quad (10)$$

The dimensional quantity Q can be regarded as a characteristic volume flow rate and it is a constant. Finally, we introduce the dimensionless time coordinate, namely in multiples of the diffusion time across the water layer,

$$\tau \equiv \frac{t - t_f}{H_w^2 / D_{\text{CO}_2}^w}, \quad (11)$$

which will mainly serve as an argument to the transient flux functions (see appendix A). The transient flux functions will be shown to be fundamental in the description of the initial transient growth of the bubble.

1. Diffusive growth

A fully developed (linear) concentration profile across the full height water layer H_w implies, by definition, a quasi-steady $Sh_w = 1$. However, there is an initial period of boundary layer development (lasting $\sim H_w^2 / 4D_{\text{CO}_2}^w$), during which $Sh_w(t)$ evolves from 0 to 1. We can formally capture the transient rate of mass transfer through the inclusion of a transient correction term $f'(\tau)$ (see appendix A). It derives from the analytical computation the diffusive flux across a layer of finite height with initial uniform zero concentration, and assuming one end of the layer (ambient interface) is at a constant concentration while the remaining end (bubble interface) remains at zero concentration. The latter assumption that $P_{\text{CO}_2}^b(t)$ remains zero is completely justified given that the fractional bubble growth is indeed small during the transient period. In such a case,

$$Sh_w = 1 - f'(\tau), \quad (12)$$

where $f'(\tau)$ is given in (A2). $Sh_w(\tau)$ is plotted in Fig. 10(a). Mass conservation implies that $\phi_b = Sh_w$. Equating (10) and (12) results in an integrable differential equation for $V_b(t)$, subject to the initial condition $V_b(t_f) = V_f$. Integration yields

$$V_b(t) = V_f \sqrt{1 + \frac{2Q}{V_f} \left[(t - t_f) - \frac{H_w^2}{D_{\text{CO}_2}^w} f(\tau) \right]}, \quad (13)$$

where the transient flux integral function $f(\tau)$ is defined in (A3) and has limits $f(0) = 0$ and $f(\infty) = 1/6$. As expected, V_b does not depend on the ambient pressure P_0 . The analytical solution (13) is plotted in Fig. 3(a) with good agreement with its experimental and numerical counterparts, (iii) and (iv).

2. Convective growth

The $Sh_w(Ra_w)$ dependence proposed in (4) can be simplified to $Sh_w = (kRa_w/Ra_c)^{1/4}$ since

$$Ra_w(t) = \frac{\lambda_{\text{CO}_2}^w S_{\text{CO}_2}^w g}{\nu_w D_{\text{CO}_2}^w} H_w^3 [P_0 - P_{\text{CO}_2}^b(t)] \quad (14)$$

is indeed large. We define $Ra_f \equiv Ra_w(t_f)$ as the initial (and maximum) Ra_w under the assumption that at t_f there is still no CO_2 in the bubble, $P_{\text{CO}_2}^b(t_f) = 0$. Thereafter, $Ra_w(t)$ has been shown to decay with bubble growth [cf. Fig. 5(b)] due to the concomitant increase in $P_{\text{CO}_2}^b(t)$. Combining the relationship in (8) with (14) gives $Ra_w(t)/Ra_f = V_f/V_b(t)$. Hence, we can relate the quasi-steady Sherwood number to the bubble volume by

$$Sh_w(t) = \beta \left(\frac{V_f}{V_b(t)} \right)^{1/4}, \quad \text{with} \quad \beta \equiv \left(\frac{kRa_f}{Ra_c} \right)^{1/4}. \quad (15)$$

The dimensionless parameter β can be regarded as the quasi-steady Sherwood number that could be potentially attained at t_f upon the immediate onset of quasi-steady convection (infinitely short transient period). Therefore,

recalling that $\delta = H_w/Sh_w$, the initial critical size of the boundary layer is set by $\delta_f = H_w/\beta$.

The initial transient regime before the onset of quasi-steady convection can be accounted for with an identical correction term as previously done in the diffusive case, except that we now consider the boundary layer development over the length δ_f instead of H_w . Accordingly, the argument of the transient functions f' in (A2) and f in (A3) is now equal to $\beta^2\tau$. The transient-corrected Sherwood number becomes

$$Sh_w(t) = \beta [1 - f'(\beta^2\tau)] \left(\frac{V_f}{V_b(t)} \right)^{1/4}. \quad (16)$$

Mass conservation implies $\phi_b = Sh_w$. Equating (10) and (16) followed by integration from $V_b(t_f) = V_f$ results in

$$V_b(t) = V_f \left[1 + \frac{9Q}{4V_f} \beta \left\{ (t - t_f) - \frac{H_w^2/D_{CO_2}^w}{\beta^2} f(\beta^2\tau) \right\} \right]^{4/9}. \quad (17)$$

The analytical solution is compared with experiments and numerical solutions in Fig. 3(a) (curves (i) and (ii)) and Fig. 5(a), displaying a very decent performance in all cases. It should be pointed out that the analytical solution intentionally shares the same fitting parameter k (i.e., through β) as its numerical counterpart, also bearing in mind that k may vary from one experiment to another within the aforementioned bounds.

V. CONVECTIVE MASS TRANSFER: SCALING

Our theoretical framework for convective dissolution is strongly based on Eq. (4) in the limit of Eq. (15), namely, on the assumption that the quasi-steady Sherwood number depends on the instantaneous Rayleigh number as $Sh_w \sim Ra_w^{1/4}$. The validity of this assumption can be verified experimentally without the need of a supporting numerical model. This requires the approximation of regarding air as insoluble. In addition, we abbreviate the pressure level $P_0(t > t_f)$ as P_0 , which is assumed to be constant. From earlier analyses (Sec. IV B), it follows that the instantaneous Rayleigh number

$$Ra_w(t) = Ra_f \frac{V_f}{V_b(t)}, \quad \text{where} \quad Ra_f \equiv \frac{\lambda_{CO_2}^w S_{CO_2}^w g}{\nu_w D_{CO_2}^w} H_w^3 P_0, \quad (18)$$

and the dimensionless bubble growth rate defined in (9)–(10) (repeated here for convenience)

$$\phi_b(t) = \frac{\dot{V}_b(t) V_b(t)}{Q \frac{V_b(t)}{V_f}}, \quad \text{where} \quad Q \equiv D_{CO_2}^w \frac{\pi d^2}{4H_w} (S_{CO_2}^w RT_0), \quad (19)$$

can both be evaluated purely from the experimental data for $t > t_f$.

The result is shown in Fig. 6, where the time-averaged ϕ_b is plotted against the time-averaged Ra_w for every single experiment. Each colored marker represents an individual binary experiment; the grey markers belong to the ternary (water–bubble–alkane) experiments and are not expected to follow Eq. (4) as will be discussed later. The time averages are computed for $t - t_f > 1100$ s to discard the initial transient growth of the bubble. The error bars indicate the range over which $\phi_b(t)$ and $Ra_w(t)$ decay during that particular experiment [cf. Fig. 5(b)]. In addition, the $Sh_w(Ra_w)$ dependence proposed in Eq. (4) is represented by the green solid curve, alongside its asymptotic slope of $1/4$. The shaded region around the curve delimits the range of the fitting parameter, $k = 2.75 \pm 1.25$, previously considered.

Figure 6(a) shows that the binary experiments fall in the asymptotic segment of the shaded $Sh_w(Ra_w)$ region. This results from mass conservation, which for the binary experiments can be expressed as $\langle \phi_b \rangle = Sh_w$, indicating that the CO_2 flux across the water layer must be equal to the CO_2 accumulation rate in the bubble. The asymptotic segment of shaded region is described by $Sh_w = a Ra_w^{1/4}$, where $a = 0.2 \pm 0.03$. Interestingly, our prefactor $a \approx 0.2$ seems to coincide with that obtained by Malkus [48] in one of the first laminar Rayleigh–Bénard convection experiments ever conducted. It is also in complete agreement with the $0.33Sc^{-1/12} \approx 0.19$ prefactor of the I_u regime of the Grossmann–Lohse theory of Rayleigh–Bénard convection in a cylindrical cell [44]. Recent experiments of CO_2 bubbles growing in carbonated water [24] suggest comparable values ($a \approx 0.3$, with the bubble radius as the relevant length scale). Dissolving sessile alcohol droplets in water [22] yield a somewhat higher exponent ($a \approx 0.6$). On the other hand, natural convection measurements over horizontal plates, at a quite different geometry, at $Pr \sim 1$ result in prefactors (based on the plate diameter) approximately fourfold larger than ours [49, 50].

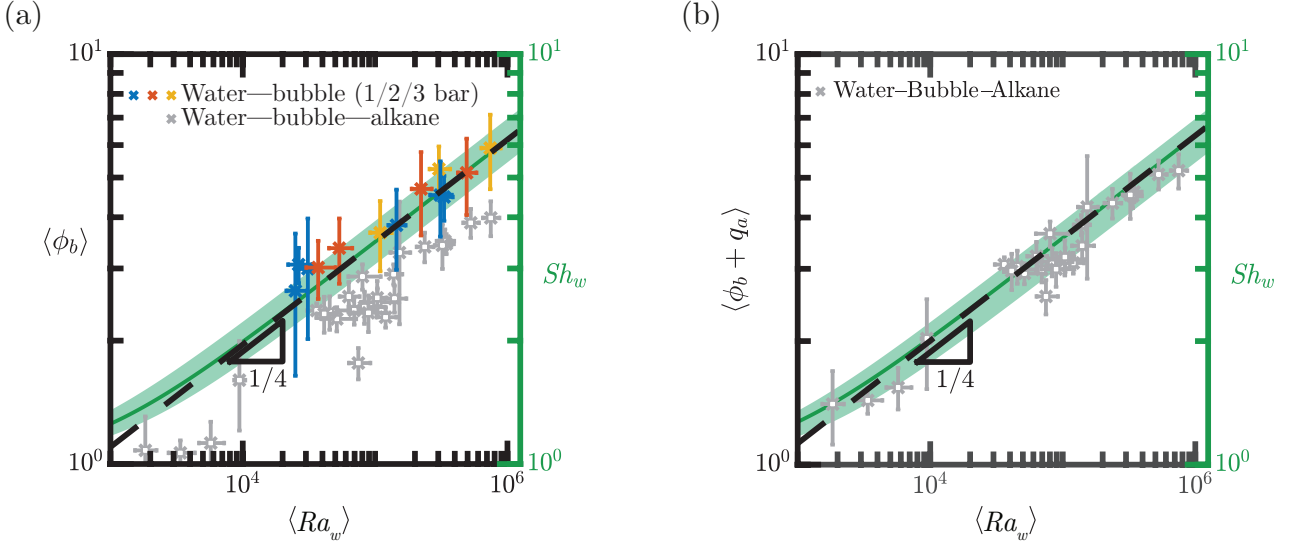


FIG. 6. (a) Time-averaged dimensionless bubble growth rate as a function of the time-averaged Ra_w for every single water–bubble experiment (colored markers) and water–bubble–alkane experiment (grey markers). The error bars indicate the range over which $\phi_b(t)$ and $Ra_w(t)$ decay during that particular experiment. The solid green line and surrounding shaded region provide the $Sh_w(Ra_w)$ dependence in (4): $Sh_w = (1 + kRa_w/Ra_c)^{1/4}$, with $k = 2.75 \pm 1.25$. (b) Bubble growth rate of the water–bubble–alkane experiments corrected with q_a , the dimensionless CO_2 leakage flux from the bubble to the alkane according to (25).

VI. WATER–BUBBLE–ALKANE SYSTEM: BUFFERING EFFECT

Next, we turn our attention to the fact all the ternary experiments fall systematically below the $Sh_w(Ra_w)$ curve in Fig. 6(a). Indeed, $\langle \phi_b \rangle < \langle Sh_w \rangle$ is a consequence of the onset of a CO_2 leakage flux from the bubble into alkane layer below. Mass conservation now reads $Sh_w = \phi_b + q_a$, where the (dimensionless) leakage flux $q_a(t)$ can be inferred purely from the experimental data under a set of simplifying assumptions. The result is shown in Fig. 6(b). Upon correcting $\langle \phi_b \rangle$ with $\langle \phi_b + q_a \rangle$, the experimental points are coherently shifted up into the $Sh_w(Ra_w)$ region.

The expression for $q_a(t)$ is provided in Eq. (25) below. It will be derived in this section, which explores the stabilising or “buffering” effect of the alkane layer on bubble growth in greater detail.

The dissolution of CO_2 into hexadecane is known to induce density gradients which similarly result in its enhanced transport [58]. Indeed, density measurements of hexadecane+ CO_2 mixtures (ρ_a) [59] and water+ CO_2 (ρ_w) mixtures [43, 60] at the same high pressure range ($P_0 > 10$ MPa) and room temperature conditions coincidentally yield a solutal expansion coefficient

$$\lambda_{\text{CO}_2}^{a/w} \equiv \left(\frac{1}{\rho_{a/w}} \frac{\partial \rho_{a/w}}{\partial C_{\text{CO}_2}^{a/w}} \right)_{P_0, T_0} \quad (20)$$

of approximately $10 \text{ cm}^3/\text{mol}$ in both cases. Note that superscript/subscript a is used to refer to the alkane (n-hexadecane) layer or medium, in the same manner as w refers to water. Since $\lambda_{\text{CO}_2}^w$ is known to depend very weakly on P_0 [43] (verified by the fact that Ref. [61] reports $\lambda_{\text{CO}_2}^w = 10.9 \text{ cm}^3/\text{mol}$ under atmospheric P_0), it is then reasonable to assume that $\lambda_{\text{CO}_2}^a \approx \lambda_{\text{CO}_2}^w$ also holds true in our low- P_0 conditions.

To determine if convective dissolution across the hexadecane layer constitutes a dominant effect, we must estimate the characteristic Rayleigh number across it, Ra_a . At the bubble–alkane interface, the surface concentration is $S_{\text{CO}_2}^a P_{\text{CO}_2}^b(t)$. At the bottom of the layer a no-flux boundary condition holds. Assuming pure diffusive transport, and provided that the increase in $P_{\text{CO}_2}^b(t)$ is sufficiently slow, the maximum (or characteristic) concentration difference across the alkane layer corresponds to that at the time t^* where self-similarity is broken therein, i.e. when the CO_2 concentration at the bottom of the alkane layer start to rise. CO_2 accumulates in the alkane layer thereon by virtue of the no-flux boundary condition. The time t^* is determined by $t^* - t_f \approx 0.3H_a^2/D_{\text{CO}_2}^a$ (see appendix A). Furthermore, we approximate air as insoluble in hexadecane, whereby $P_b = P_0 \Delta V_b/V_b$ from (8) applies.

The resulting expression for Ra_a can be insightfully deployed in relation to the maximum Rayleigh number across the

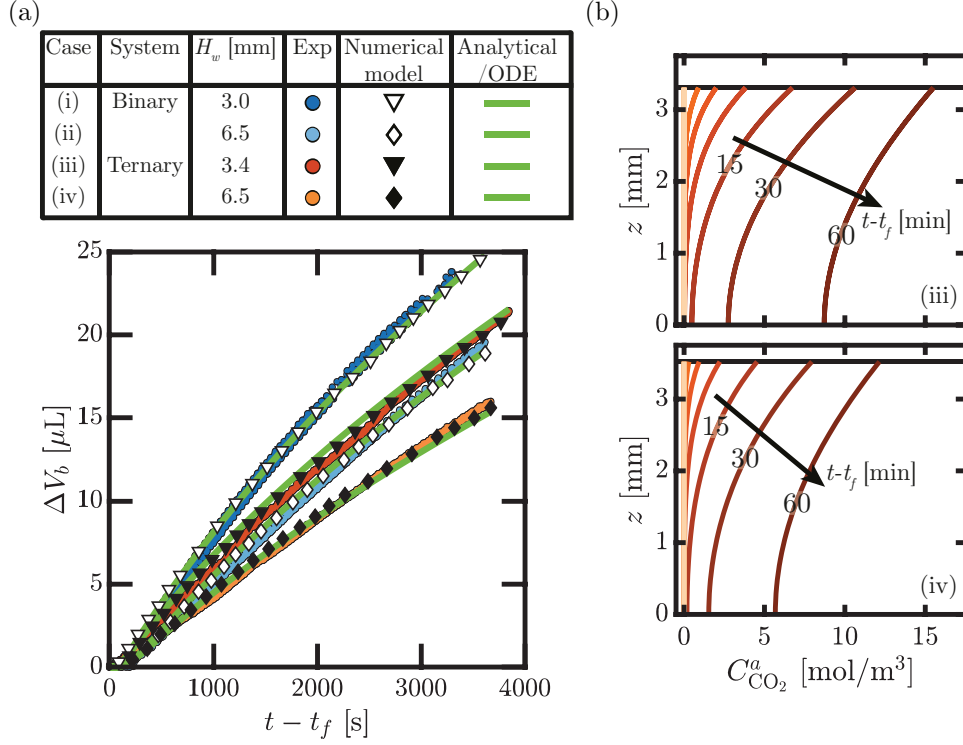


FIG. 7. (a) Comparison of the bubble growth dynamics for water–bubble system (cases i, ii) and ternary water–bubble–alkane systems (cases ii, iv) for two distinct water layer heights. The alkane layer height is $H_a \approx 3.5$ mm. In all four cases, $V_f = 35 \mu\text{L}$ and $P_0 = 1$ bar. Experiments (i, ii) are overlaid with numerical and analytical (17) solutions; experiments (iii, iv) with numerical and ODE (27) solutions. (b) Time evolution of the CO₂ concentration profile in the alkane layer according to the numerical model for case (iii) [top panel] and case (iv)[bottom panel].

water layer, Ra_f [see Eq. (18)]. Neglecting the small differences in the solubilities, diffusivities and solutal expansion coefficients of CO₂ in water and in hexadecane (see Table I), we can write

$$\frac{Ra_a}{Ra_f} \approx \frac{\Delta V_b}{V_b} \frac{H_a \nu_w}{H_w \nu_a}. \quad (21)$$

For a typical experiment with $V_f = 35 \mu\text{L}$ and $H_a = 3$ mm, we find $(t^* - t_f) \sim 1,200$ s and, from earlier figures, $\Delta V_b(t^*) \approx 5 \mu\text{L}$, hence $\Delta V_b(t^*)/V_b(t^*) \approx 1/8$. Taking $H_w \approx H_a$, and noting that $\nu_w/\nu_a \approx 1/4$, we finally obtain a characteristic magnitude of $Ra_a/Ra_f \sim 3\%$. This always translates to $Ra_a < 10^4$, i.e., $Ra_a \sim Ra_c$ at most. Therefore, under the current experimental conditions, diffusion can be safely assumed to remain the dominant transport mechanism across the alkane layer. The numerical model can then be straightforwardly extended to incorporate the presence of the alkane layer (see appendix B), by solving the one-dimensional diffusion equation for all three species ($j = \text{CO}_2, \text{O}_2$ and N_2) over the whole height of the alkane layer. The resulting interfacial fluxes from the bubble to the alkane, J_j^{ba} , modify mass conservation to $J_j^{wb} - J_j^{ba} = 4\dot{n}_j^b/\pi d^2$ (cf. the discussion above Eq. (2)).

Figure 7(a) compares the bubble growth dynamics of two binary experiments at $P_0(t > t_f) = 1$ bar [same cases (i) and (ii) from Fig. 3] with their equivalent ternary systems with $H_a \approx 3.5$ mm under otherwise the same conditions. The buffering effect of the n-hexadecane layer on bubble growth first introduced in Fig. 2 is clearly observed again. The good performance of the numerical solution validates, once more, the assumption of negligible convective dissolution across the alkane layer. On another note, the transient nature of $J_j^{ba}(t)$ can be inferred from the time evolution of the numerical CO₂ concentration profiles in the alkane layer shown in Fig. 7(b). Quasi-steady or self-similar profiles or fluxes are never attained. This is a consequence of the unsteady interfacial concentration $C_{CO_2}^a(H_a, t)$ being strictly an increasing function of time and the no-flux boundary condition on $z = 0$. Notice that CO₂ starts accumulating in the alkane layer after a time of approximately 15 minutes, in accordance with our previous estimation.

The added analytical complexity brought by the transient nature of the CO₂ transport across the alkane layer can be witnessed, for example, in the unmanageable time-integral-laden mathematical expression of the concentration profile across a finite sheet subject to a no-flux boundary condition and variable surface concentration [62]. However,

noting that on the time scale of our experiments the hexadecane layer hardly becomes saturated [cf. Fig. 7(b)], we may choose to ignore the effect of the no-flux boundary. We do so by treating the hexadecane layer as a semi-infinite medium. Not only is this a reasonable simplification, it also poses a problem of particular interest. In such a case, and treating air as insoluble, we can reduce the model formulation to a single ordinary differential equation for $V_b(t)$ as will be shown in the next subsection.

A. Dynamic equation for bubble growth

Approximating air as insoluble renders Eq. (8) which allows us to relate the surface concentration of CO_2 in the alkane layer at the alkane–bubble interface to the instantaneous bubble volume by

$$C_s(t) = S_{\text{CO}_2}^a P_{\text{CO}_2}^b(t) = S_{\text{CO}_2}^a P_0 \left[1 - \frac{V_f}{V_b(t)} \right], \quad (22)$$

where P_0 here abbreviates the constant pressure level $P_0(t > t_f)$. It should be noted that, unlike in water, the solubilities of air and CO_2 in n-hexadecane are quite comparable (see Table I). Therefore, the approximation of neglecting the flux of air into the hexadecane layer is mostly valid for $P_0 = 1$ bar because the hexadecane layer is initially saturated with air at that pressure. Pressurisation beyond this value results in the immediate undersaturation of the later; raising P_0 further eventually yields fluxes of air and CO_2 of similar magnitude.

Next, treating the alkane layer as semi-infinite fully removes the length scale H_a from the problem, which allows us to conveniently work with the water-layer time τ defined in Eq. (11) instead. The CO_2 diffusion flux from the bubble to the semi-infinite alkane layer with a time-dependent surface concentration is given by (see e.g. Ref. [63])

$$J_{\text{CO}_2}^{ba} = \frac{D_{\text{CO}_2}^a}{H_w} \left[\frac{1}{\sqrt{\pi}} \int_0^\tau \frac{1}{\sqrt{\tau - u}} \frac{dC_s}{du} du \right] \quad (23)$$

Identical history integral flux terms to the one above can be found deployed in previous analytical treatments concerning the growth and dissolution of drops/bubbles with unsteady surface concentrations [64, 65]. The integral describes the so-called history effect, i.e., the contribution of past mass transfer events on the current growth dynamics. The fact that the recent history contributes the most, $1/\sqrt{\tau - u} \rightarrow \infty$ as $u \rightarrow \tau$, can be used to evaluate the time integral in our case. Since the bubble growth dynamics are quite steady (no abrupt or fast changes in \dot{V}_b), we can approximate dC_s/du as the current time derivative $dC_s(\tau)/d\tau$ irrespective of u . Analytical integration is then possible, and the flux becomes

$$J_{\text{CO}_2}^{ba} = \frac{D_{\text{CO}_2}^a}{H_w} \left[2\sqrt{\tau} \frac{dC_s}{d\tau} \right] = \left(\frac{2D_{\text{CO}_2}^a S_{\text{CO}_2}^a P_0 V_f}{\sqrt{\pi} D_{\text{CO}_2}^w} \right) \frac{\dot{V}_b(t)}{V_b(t)^2} \sqrt{t - t_f}, \quad (24)$$

where use of Eq. (11) and Eq. (22) has been made. The dimensionless flux, q_a , into the alkane (normalised by the water-layer diffusive flux, in coherence with Sh_w and ϕ_b) is

$$q_a(t) \equiv \frac{J_{\text{CO}_2}^{ba}(t) H_w}{D_{\text{CO}_2}^w \Delta C_{\text{CO}_2}^w(t)} = \sqrt{T^{aw}} \sqrt{t - t_f} \frac{\dot{V}_b}{V_b}, \quad \text{with} \quad \sqrt{T^{aw}} = \frac{2H_w}{\sqrt{\pi} D_{\text{CO}_2}^w} \frac{D_{\text{CO}_2}^a S_{\text{CO}_2}^a}{D_{\text{CO}_2}^w S_{\text{CO}_2}^w}. \quad (25)$$

Here T^{aw} is a time constant which depends purely on the system properties. The remaining ingredients have been derived in Sec. IV B; these are naturally ϕ_b and Sh_w , whose expressions are given in Eq. (9) and Eq. (16) respectively. Finally, mass conservation yields

$$\phi_b = Sh_w - q_a. \quad (26)$$

Substituting the expressions in Eq. (9), Eq. (16) and Eq. (25), the mass balance becomes

$$\frac{\dot{V}_b}{Q} \frac{V_b}{V_f} = \left\{ \beta [1 - f'(\beta^2 \tau)] \left(\frac{V_f}{V_b} \right)^{1/4} \right\} - \left\{ \sqrt{T^{aw}} \sqrt{t - t_f} \frac{\dot{V}_b}{V_b} \right\}, \quad (27)$$

which constitutes an ordinary nonlinear differential equation for $V_b(t > t_f)$ that can be numerically integrated subject to the initial condition $V_b(t_f) = V_f$. The solution to (27) is plotted in Fig. 7(a) for cases (iii) and (iv), where the ODE solution shares the same fitting coefficient k as its numerical counterpart. Overall, excellent agreement is observed,

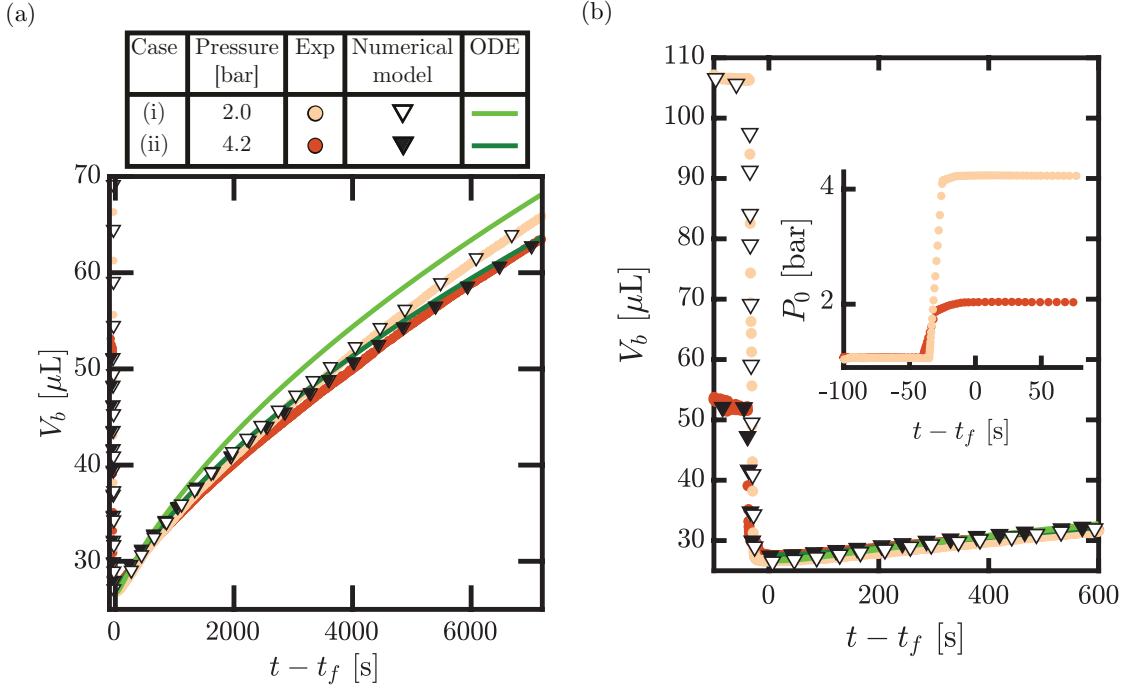


FIG. 8. (a) Bubble growth dynamics for the water–bubble–alkane system at higher pressure levels ($V_f = 27\mu\text{L}$). Case (i): $P_0 = 2.0$ bar, $H_w = 3.0$ mm, $H_a = 3.2$ mm; case (ii) $P_0 = 4.2$ bar, $H_w = 3.0$ mm, $H_a = 3.2$ mm. Experimental, numerical and ODE (27) results are compared. (b) Close-up of the pressurisation stage and initial growth. Inset: Concomitant pressure time history.

despite the underlying simplifications. We also point out that the flux $q_a(t)$ in Eq. (25) is independent of k (or any other fitting parameter) and it can be evaluated directly from the experimental measurements, as done for Fig. 6(b).

Figure 8(a) shows the bubble growth dynamics of the water–bubble–alkane system ($H_w \approx H_a \approx 3$ mm) at higher experiment pressure levels, namely at $P_0 = 2.0$ and 4.2 bar. Interestingly, the alkane buffering effect also visibly diminishes the dependence of the growth rate V_b on P_0 . The separation of the growth curves is indeed less pronounced than in the binary system, see Fig. 5(a). The limitation of the ODE solution becomes apparent at these higher pressures. The ODE overestimates the growth rate, a consequence of neglecting the dissolution flux of air from the bubble into the alkane. The deviation worsens with increasing P_0 , i.e., with the air flux magnitude. On another note, the accuracy of the numerical model in reproducing the initial pressure-bound dynamics is highlighted in Fig. 8(b), which shows a close-up of the initial minutes of bubble growth and the preceding pressurisation stage. Bubble dissolution for $t > t_f$ is not observed, despite the fact that the dissolution flux of air into the alkane is strongest at $t \approx t_f$. The onset of convective dissolution is as fast as the time required for the step in pressure to reach and stabilise at the experiment level [see Fig. 8(b) inset].

B. Nitrogen solute exchange

To further visualise the buffering effect of the hexadecane layer on bubble dissolution, a two-cylinder experiment consisting of a binary and ternary system ($V_f = 35\mu\text{L}$, $H_w = 3$ mm and $H_a = 3$ mm) was placed in a CO_2 atmosphere at $P_0(t > t_f) = 1.0$ bar. After 1 hour, the CO_2 atmosphere is replaced by a N_2 atmosphere at the same pressure. The resulting bubble dynamics are shown in Fig. 9. The first solute exchange event induces bubble growth, as discussed extensively in the previous sections. In contrast, the second solute exchange induces bubble dissolution, as CO_2 from the bubbles redissolves back through the water barrier. Note that the opposing N_2 flux is much weaker owing to its poor solubility in water. The buffering effect of the alkane layer stands out with the fact that the bubble in the ternary system shrinks slower compared to the bubble in the bubble–water system. This difference is caused by CO_2 exsolving from the alkane back into the bubble. After replacing the CO_2 atmosphere with N_2 , the CO_2 concentration gradient across the water layer is effectively inverted. The dense CO_2 -rich boundary layer now rests at the bottom water–

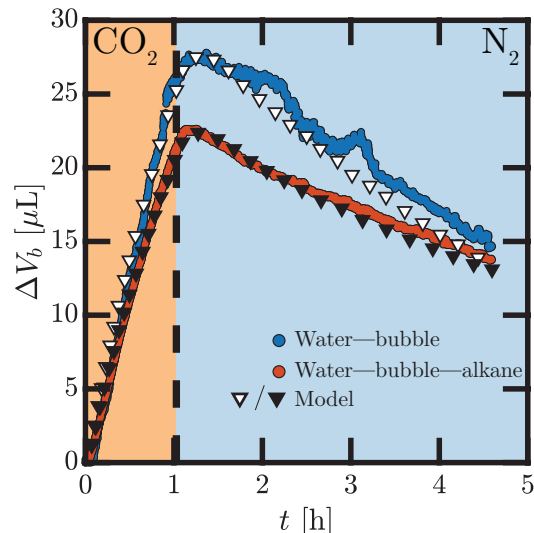


FIG. 9. Bubble growth dynamics for a binary and ternary system ($V_f = 35 \mu\text{L}$, $H_w = 3 \text{ mm}$ and $H_a = 3 \text{ mm}$) at $P_0 = 1 \text{ bar}$. After $t = 1 \text{ h}$, the CO_2 atmosphere inside the chamber is replaced by a N_2 atmosphere at the same pressure, thereby enforcing dissolution.

bubble interface. Stratification is stable thereon, and therefore the transport of CO_2 can be assumed to be purely driven by diffusion. This evidently results in a slower dissolution rate. The model prediction importantly reflects the asymmetry between the growth and dissolution stages, and overlaps reasonably well with the experimental results.

VII. CONCLUSIONS & OUTLOOK

We have investigated the growth dynamics of a trapped slug bubble in a vertical glass cylinder beneath a short layer of water which separates the bubble from the ambient gas. Replacing the ambient air with a CO_2 atmosphere induces an asymmetric exchange of the gaseous solutes between the CO_2 -rich water barrier and the air-rich bubble. Net bubble growth is always observed, even after pressurisation. We refer to this process as solute exchange.

The dominant transport of CO_2 across the water barrier is facilitated by diffusion and greatly enhanced by convective dissolution. Inverting the cylinder orientation has correspondingly been shown to suppress convection. The transport of CO_2 across the layer was then fully driven by diffusion, resulting in slower growth. The bubble growth dynamics and underlying mass transport processes were characterised by means of a numerical model based on one-dimensional diffusive transport. Analytical solutions able to accurately predict the growth dynamics were subsequently derived. The effect of convective dissolution across the water layer was treated as a reduction of the effective diffusion length, in accordance with the expected scaling for laminar or natural convection. The fact that the Sherwood number scales to the $1/4$ power of the Rayleigh number was verified experimentally, and explains why the bubble growth rate was observed to increase with the ambient pressure but behaves inversely with the the water layer height.

Finally, the binary water–bubble system was compared to a ternary water–bubble–alkane system. The alkane (n-hexadecane) layer was shown to act essentially as an unsteady sink (or source) of CO_2 gas. As a result, the alkane layer induces a buffering effect on the bubble growth (or dissolution) dynamics. The slower growth curves were well reproduced by an extension of the numerical model and ultimately a single dynamical equation for the bubble volume derived under a set of simplifying assumptions.

Our findings offer new insight on mass-transfer effects in microfluidic or microreactor devices comprising segmented gas–liquid phases or density-changing solutes, and also on the growth and elimination of trapped bubbles. Moreover, the differences in the growth rates between binary systems, ternary systems, or a combination thereof, can offer a feasible means by which the physical properties of gases in the liquid layers can be obtained.

ACKNOWLEDGEMENTS

This work was supported by the Netherlands Center for Multiscale Catalytic Energy Conversion (MCEC), an NWO Gravitation programme funded by the Ministry of Education, Culture and Science of the government of the Netherlands.

Appendix A: Diffusion across a sheet of finite length

Consider the canonical problem of one-dimensional diffusion across a sheet of finite length. One end of the sheet is kept at a constant surface concentration while the remaining end is at zero concentration. The sheet concentration profile is initially zero. With proper normalisation, the dimensionless problem considers a surface concentration, diffusivity and sheet length of unity. Our particular case involves the diffusion of $C_{\text{CO}_2}^w(z, t > t_f)$ across a water layer of height H_w with surface concentrations $C_{\text{CO}_2}^w(H_w, t) = S_{\text{CO}_2}^w P_0$ and $C_{\text{CO}_2}^w(0, t) = 0$. We then consider $c = C_{\text{CO}_2}^w/S_{\text{CO}_2}^w P_0$ as a function of $\xi = 1 - z/H_w$ and $\tau = D_{\text{CO}_2}^w(t - t_f)/H_w^2$.

The solution to $\partial_\tau c = \partial_{\xi\xi} c$ subject to $c(0, \tau) = 1$, $c(1, \tau) = 0$ and $c(\xi, 0) = 0$ is (see e.g. Ref. [66])

$$c(\xi, \tau) = (1 - \xi) - \frac{2}{\pi} \sum_{n=1}^{\infty} \frac{1}{n} \sin(n\pi\xi) e^{-n^2\pi^2\tau}. \quad (\text{A1})$$

Fluxes can be easily deduced from (A1). At any given time, the diffusion flux out of the sheet (across the zero-concentration end) is $-\partial_\xi c(\xi, \tau)|_{\xi=1} = 1 - f'(\tau)$, where

$$f'(\tau) = -2 \sum_{n=1}^{\infty} (-1)^n e^{-n^2\pi^2\tau} \quad (\text{A2})$$

is referred to as the transient flux function. It has limits $f'(\infty) = 0$ and $f'(\tau \rightarrow 0) = 1$ but $f'(0)$ is non-analytical in $\tau = 0$. The diffusion flux $1 - f'(\tau)$ is plotted in Fig. 10(a) and it is equivalent to our Sherwood number given that it precisely quantifies mass transfer out of the sheet. This result is directly used in (12).

Figure 10(a) also plots the total amount of substance that has diffused out in time τ , namely $\tau - f(\tau)$, where

$$f(\tau) \equiv \frac{1}{6} + \frac{2}{\pi^2} \sum_{n=1}^{\infty} \frac{(-1)^n}{n^2} e^{-n^2\pi^2\tau}, \quad (\text{A3})$$

is referred to as the transient flux integral function. It has limits $f(0) = 0$, and $f(\infty) = 1/6$.

In the limit $\tau \rightarrow 0$, (A1) converges to the self-similar solution $c_{ss}(\xi, \tau) = \text{erfc}(\xi/\sqrt{4\tau})$. The time at which self-similarity is broken can be estimated as the time at which the finite length of the sheet causes the influx (on $\xi = 0$) to deviate from the self-similar solution by an arbitrary fractional amount. This is done in Fig. 10(b), which plots the ratio of the influx of the self-similar solution, $q_{ss} = 1/\sqrt{\pi\tau}$, to the influx of the solution in (A1), namely

$$q = 1 + 2 \sum_{n=1}^{\infty} e^{-n^2\pi^2\tau}. \quad (\text{A4})$$

This result is relevant in the description of the diffusive transport in the water layer. In the case of the alkane layer, we should consider the diffusion across an equivalent sheet where the zero-concentration boundary $c(1, \tau) = 0$ is replaced by a no-flux boundary, i.e., $\partial c/\partial\xi = 0$ on $\xi = 1$. The influx (on $\xi = 0$) becomes (see e.g. Ref. [66])

$$q_{nf} = 2 \sum_{n=0}^{\infty} \exp \left[-\pi^2 \left(n + \frac{1}{2} \right)^2 \tau \right]. \quad (\text{A5})$$

Similarly, the time at which self-similarity is broken can be estimated as the time in which $q_{nf}/q_{ss} \leq 1$ falls below an arbitrary threshold, see Fig. 10(b).

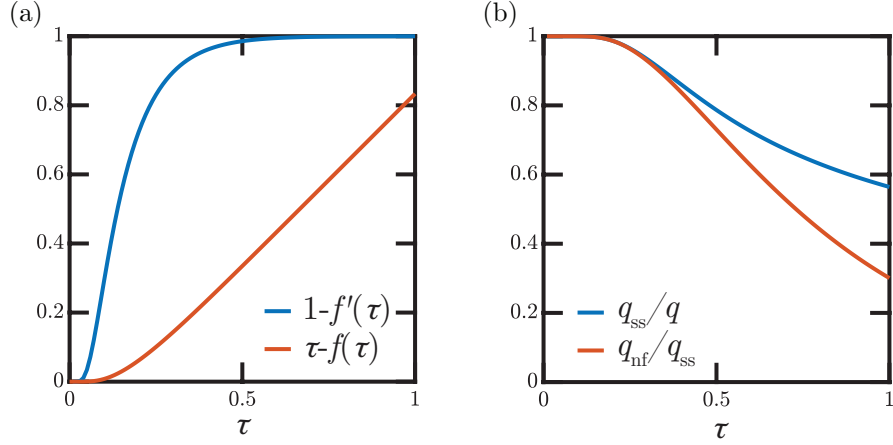


FIG. 10. (a) Diffusion outflux (blue line) and its time integral (red line) as functions of time. The transient period can be thought to last $\tau \sim 0.4$, after which the flux overcomes the 95 % mark of the steady-state value. (b) Influx ratios: q_{ss} denotes the (self-similar) diffusion influx into the unit-concentration boundary of an infinite sheet, q is the influx into the unit-concentration boundary of a sheet of unit length delimited by a zero-concentration boundary, and q_{nf} is the influx into the unit-concentration boundary of a sheet of unit length delimited by a no-flux boundary. In both cases, self-similarity breaks down after a time $\tau \sim 0.3$, where the flux ratios drop below 95 %.

Appendix B: One-dimensional numerical model

Following the notation of main text, the quantities associated with the water phase are indicated by subscript/superscript w ; subscript/superscript b refers to the bubble, a to the alkane and 0 to the ambient. The transport of molar concentration of gas species $j = \text{CO}_2, \text{O}_2$ or N_2 dissolved in the water layer is modelled by the 1D diffusion equation,

$$\frac{\partial C_j^w}{\partial t} = D_j^w \frac{\partial^2 C_j^w}{\partial x^2}, \quad \text{on } 0 < x < H_w. \quad (\text{B1})$$

The concentration boundary conditions in the water phase follow Henry's law,

$$C_j^w(0, t) = S_j^w P_j^b(t), \quad C_j^w(H_w, t) = S_j^w X_j^0(t) P_0(t), \quad (\text{B2})$$

where the ambient pressure $P_0(t)$ and ambient mole fractions, $X_j^0(t)$ are prescribed at all times. In our case, the pressure history $P_0(t)$ is directly interpolated from the experimental measurements. In the presence of dissolution-driven convection, we must solve for $C_{\text{CO}_2}^w$ within a single diffusive region (boundary layer) of length $\delta(t)$ as explained in the main text, that is

$$\frac{\partial C_{\text{CO}_2}^w}{\partial t} = D_{\text{CO}_2}^w \frac{\partial^2 C_{\text{CO}_2}^w}{\partial \xi^2} \quad \text{on } 0 < \xi < \delta(t). \quad (\text{B3})$$

The numerical difficulties inherent in solving the moving-boundary problem posed in (B3) can be circumvented by introducing a coordinate transformation $x(t) = H_w \xi / 2\delta(t)$ which reverts the spatial domain back to $0 \leq x \leq H_w$. We then solve for $C_{\text{CO}_2}^w(x, t)$ from

$$\frac{\partial C_{\text{CO}_2}^w}{\partial t} - \frac{\dot{\delta}}{\delta} x \frac{\partial C_{\text{CO}_2}^w}{\partial x} = D_{\text{CO}_2}^w \left(\frac{H_w}{\delta} \right)^2 \frac{\partial^2 C_{\text{CO}_2}^w}{\partial x^2} \quad \text{on } 0 < x < H_w. \quad (\text{B4})$$

The boundary conditions in (B2) therefore still apply. Note that a numerical advection term [second term in the left-hand-side of (B4)] formally appears as a consequence of the coordinate $x(t)$ changing with time. It is however neglected under the assumption that the variations in δ are slow as compared to diffusion, i.e., $\dot{\delta}/D_{\text{CO}_2}^w \ll 1$. The thickness δ is computed at every time step as established by the relationship in (5), where the numerical value of $Ra_w(t)$ [as defined in (3)] is evaluated at the previous time step.

When modelling the ternary water–bubble–alkane system, we must additionally solve the diffusion equation in the

alkane layer,

$$\frac{\partial C_j^a}{\partial t} = D_j^a \frac{\partial^2 C_j^a}{\partial y^2}, \quad \text{on } 0 < y < H_a, \quad (\text{B5})$$

with boundary conditions

$$\frac{\partial C_j^a}{\partial y}(0, t) = 0, \quad C_j^a(H_a, t) = S_j^a P_j^b(t). \quad (\text{B6})$$

The partial pressures inside the bubble are assumed proportional to the mole fractions, $P_j^b = n_j^b P_b / n_b$, where $n_b(t) = \sum_j n_j^b(t)$ is the total number of moles of gas and the assumption $P_b(t) = P_0(t)$ neglects the Laplace pressure in the bubble. The gas content in the bubble is found by integrating in time the molar fluxes into the bubble,

$$\frac{4}{\pi d^2} \frac{dn_j^b}{dt} = D_j^w \frac{\partial C_j^w}{\partial x}(x=0, t) - D_j^a \frac{\partial C_j^a}{\partial y}(y=H_a, t). \quad (\text{B7})$$

Finally, the bubble volume is assumed to evolve according to the ideal gas law, $P_0(t)V_b(t) = n_b(t)RT_0$. Before flushing ($t < t_{f-start}$), the system is in thermodynamic equilibrium. The initial bubble volume is $V_b(t < t_{f-start}) = V_{eq}$ and $P_0(t < t_{f-start}) = P_{eq}$. The initial conditions read

$$\begin{aligned} C_j^a(x, t < t_{f-start}) &= S_j^a P_{eq} X_j^{0,eq}, \\ C_j^w(y, t < t_{f-start}) &= S_j^w X_j^{0,eq} P_{eq} \end{aligned} \quad (\text{B8})$$

and

$$n_j^b(t < t_{f-start}) = \frac{P_{eq} X_j^{0,eq} V_{eq}}{RT_0} \quad (\text{B9})$$

where $X_{\text{CO}_2}^{0,eq} = 0$, $X_{\text{N}_2}^{0,eq} = 0.79$ and $X_{\text{O}_2}^{0,eq} = 0.21$ is the composition of dry air. Immediately upon flushing ($t > t_{f-start}$), the ambient composition is set to reflect a pure CO₂ atmosphere: $X_{\text{CO}_2}^0 = 1$, and $X_{\text{N}_2}^0 = X_{\text{O}_2}^0 = 0$. The diffusion equations are discretized using a second-order central finite-differences scheme. The resulting ODE system for $C_j^w(x, t)$, $C_j^a(y, t)$ and $n_j^b(t)$ is integrated in time with a standard Runge–Kutta ODE solver.

-
- [1] L. Jiang, Z. Xue, and H. Park, Enhancement of CO₂ dissolution and sweep efficiency in saline aquifer by microbubble CO₂ injection, *Int. J. Heat Mass Transf.* **138**, 1211 (2019).
 - [2] H. E. Huppert and J. A. Neufeld, The fluid mechanics of carbon dioxide sequestration, *Annu. Rev. Fluid Mech.* **46**, 255 (2014).
 - [3] J. B. Grotberg, Respiratory fluid mechanics, *Phys. Fluids* **23**, 021301 (2011).
 - [4] Y. Cao, C. Soares, N. Padoin, and T. Noël, Gas bubbles have controversial effects on Taylor flow electrochemistry, *Chem. Eng. J.* **406**, 126811 (2021).
 - [5] M. Abolhasani, A. Günther, and E. Kumacheva, Microfluidic studies of carbon dioxide, *Angew. Chem. Int. Edit.* **53**, 7992 (2014).
 - [6] T. Cubaud, M. Sauzade, and R. Sun, CO₂ dissolution in water using long serpentine microchannels, *Biomicrofluidics* **6**, 022002 (2012).
 - [7] T. Lu, R. Fan, L. F. Delgadillo, and J. Wan, Stabilization of carbon dioxide (CO₂) bubbles in micrometer-diameter aqueous droplets and the formation of hollow microparticles, *Lab on a Chip* **16**, 1587 (2016).
 - [8] E. Stride and M. Edirisinghe, Novel microbubble preparation technologies, *Soft Matter* **4**, 2350 (2008).
 - [9] I. Pereiro, A. F. Khartchenko, L. Petrini, and G. V. Kaigala, Nip the bubble in the bud: a guide to avoid gas nucleation in microfluidics, *Lab Chip* **19**, 2296 (2019).
 - [10] A. Volk, M. Rossi, C. J. Kähler, S. Hilgenfeldt, and A. Marin, Growth control of sessile microbubbles in PDMS devices, *Lab Chip* **15**, 4607 (2015).
 - [11] R. B. Espinosa, M. H. Duits, D. Wijnperlé, F. Mugele, and L. Lefferts, Bubble formation in catalyst pores; curse or blessing?, *React. Chem. Eng.* **3**, 826 (2018).
 - [12] S. Prakash, W. Mustain, and P. A. Kohl, Carbon dioxide vent for direct methanol fuel cells, *J. Power Sources* **185**, 392 (2008).

- [13] D. D. Meng, T. Cubaud, C. Ho, and C. Kim, A methanol-tolerant gas-venting microchannel for a microdirect methanol fuel cell, *Journal of Microelectromechanical Systems* **16**, 1403 (2007).
- [14] C. Litterst, S. Eccarius, C. Hebling, R. Zengerle, and P. Koltay, Increasing μ dmfc efficiency by passive CO₂ bubble removal and discontinuous operation, *J. Micromech. Microeng.* **16**, S248 (2006).
- [15] N. Pande, S. K. Chandrasekar, D. Lohse, G. Mul, J. A. Wood, B. T. Mei, and D. Krug, Electrochemically induced pH change: Time-resolved confocal fluorescence microscopy measurements and comparison with numerical model, *J. Phys. Chem. Lett.* **11**, 7042 (2020).
- [16] D. Lohse, Fundamental fluid dynamics challenges in inkjet printing, *Annu. Rev. Fluid Mech.* **54**, 1 (2022).
- [17] D. Lohse, Bubble puzzles: From fundamentals to applications, *Phys. Rev. Fluids* **3**, 110504 (2018).
- [18] S. Peng, T. L. Mega, and X. Zhang, Collective effects in microbubble growth by solvent exchange, *Langmuir* **32**, 11265 (2016).
- [19] Z. Lu, H. Xu, H. Zeng, and X. Zhang, Solvent effects on the formation of surface nanodroplets by solvent exchange, *Langmuir* **31**, 12120 (2015).
- [20] M. C. Rogers and S. W. Morris, Buoyant plumes and vortex rings in an autocatalytic chemical reaction, *Phys. Rev. Lett.* **95**, 024505 (2005).
- [21] V. Loodts, H. Saghrou, B. Knaepen, L. Rongy, and A. De Wit, Differential diffusivity effects in reactive convective dissolution, *Fluids* **3**, 83 (2018).
- [22] E. Dietrich, S. Wildeman, C. W. Visser, K. Hofhuis, E. S. Kooij, H. J. W. Zandvliet, and D. Lohse, Role of natural convection in the dissolution of sessile droplets, *J. Fluid Mech.* **794**, 45 (2016).
- [23] K. L. Chong, Y. Li, C. S. Ng, R. Verzicco, and D. Lohse, Convection-dominated dissolution for single and multiple immersed sessile droplets, *J. Fluid Mech.* **892**, A21 (2020).
- [24] Á. Moreno Soto, O. R. Enríquez, A. Prosperetti, D. Lohse, and D. van der Meer, Transition to convection in single bubble diffusive growth, *J. Fluid Mech.* **871**, 332 (2019).
- [25] G. Ahlers, S. Grossmann, and D. Lohse, Heat transfer and large scale dynamics in turbulent Rayleigh-Bénard convection, *Rev. Mod. Phys.* **81**, 503 (2009).
- [26] C. Yao, Y. Liu, S. Zhao, Z. Dong, and G. Chen, Bubble/droplet formation and mass transfer during gas-liquid-liquid segmented flow with soluble gas in a microchannel, *AIChE J.* **63**, 1727 (2017).
- [27] K. Sklodowska and S. Jakiela, Enhancement of bacterial growth with the help of immiscible oxygenated oils, *RSC Adv.* **7**, 40990 (2017).
- [28] R. Sander, Compilation of Henry's law constants (version 4.0) for water as solvent, *Atmos. Chem. Phys.* **15**, 4399 (2015).
- [29] F. L. Smith and A. H. Harvey, Avoid common pitfalls when using henry's law, *Chem. Eng. Prog.* **103**, 33 (2007).
- [30] J. Makranczy, K. M. Megyery-Balog, L. Ruzs, and L. Patyi, Solubility of gases in normal-alkanes, *HJIC* **4**, 269 (1976).
- [31] O. R. Enríquez, C. Hummelink, G.-W. Bruggert, D. Lohse, A. Prosperetti, D. van der Meer, and C. Sun, Growing bubbles in a slightly supersaturated liquid solution, *Rev. Sci. Instrum.* **84**, 065111 (2013).
- [32] B.-S. Chun and G. T. Wilkinson, Interfacial tension in high-pressure carbon dioxide mixtures, *Industrial & Engineering Chemistry Research* **34**, 4371 (1995).
- [33] A. Tamimi, E. B. Rinker, and O. C. Sandall, Diffusion coefficients for hydrogen sulfide, carbon dioxide, and nitrous oxide in water over the temperature range 293-368 K, *J. Chem. Eng. Data* **39**, 330 (1994).
- [34] J. B. Matthews, Michael A. Rodden and A. Akgerman, High-temperature diffusion, viscosity, and density measurements in n-hexadecane, *J. Chem. Eng. Data* **32**, 317 (1987).
- [35] I. Zandi and C. D. Turner, The absorption of oxygen by dilute polymeric solutions molecular diffusivity measurements, *Chem. Eng. Sci.* **25**, 517 (1970).
- [36] L.-K. Ju and C. S. Ho, Oxygen diffusion coefficient and solubility in n-hexadecane, *Biotechnol. Bioeng.* **34**, 1221 (1989).
- [37] D. M. Himmelblau, Diffusion of dissolved gases in liquids, *Chem. Rev.* **64**, 527 (1964).
- [38] S. Backhaus, K. Turitsyn, and R. E. Ecke, Convective instability and mass transport of diffusion layers in a Hele-Shaw geometry, *Phys. Rev. Lett.* **106**, 104501 (2011).
- [39] B. Arendt, D. Dittmar, and R. Eggers, Interaction of interfacial convection and mass transfer effects in the system CO₂-water, *Int. J. Heat Mass Transf.* **47**, 3649 (2004).
- [40] A. C. Slim, M. M. Bandi, J. C. Miller, and L. Mahadevan, Dissolution-driven convection in a Hele-Shaw cell, *Phys. Fluids* **25**, 024101 (2013).
- [41] R. Farajzadeh, H. Salimi, P. L. J. Zitha, and H. Bruining, Numerical simulation of density-driven natural convection in porous media with application for CO₂ injection projects, *Int. J. Heat Mass Transf.* **50**, 5054 (2007).
- [42] V. Loodts, L. Rongy, and A. De Wit, Impact of pressure, salt concentration, and temperature on the convective dissolution of carbon dioxide in aqueous solutions, *Chaos* **24**, 043120 (2014).
- [43] J. E. Garcia, *Density of aqueous solutions of CO₂*, Tech. Rep. (Lawrence Berkeley National Laboratory, 2001).
- [44] S. Grossmann and D. Lohse, Scaling in thermal convection: a unifying theory, *J. Fluid Mech.* **407**, 27 (2000).
- [45] A. Bejan, *Convection heat transfer* (John Wiley & Sons, 2013).
- [46] T. J. Kneafsey and K. Pruess, Laboratory experiments and numerical simulation studies of convectively enhanced carbon dioxide dissolution, *Energy Procedia* **4**, 5114 (2011).
- [47] F. Hébert, R. Hufschmid, J. Scheel, and G. Ahlers, Onset of Rayleigh-Bénard convection in cylindrical containers, *Phys. Rev. E* **81**, 046318 (2010).
- [48] W. V. R. Malkus, Discrete transitions in turbulent convection, *Proc. Math. Phys. Eng. Sci.* **225**, 185 (1954).
- [49] R. J. Goldstein, E. M. Sparrow, and D. C. Jones, Natural convection mass transfer adjacent to horizontal plates, *Int. J.*

- Heat Mass Transf. **16**, 1025 (1973).
- [50] J. R. Lloyd and W. R. Moran, Natural Convection Adjacent to Horizontal Surface of Various Planforms, *J. Heat Transfer* **96**, 443 (1974).
- [51] G. O. Roberts, Fast viscous Bénard convection, *Geophys. Astrophys. Fluid Dyn.* **12**, 235 (1979).
- [52] M. Vynnycky and Y. Masuda, Rayleigh-Bénard convection at high Rayleigh number and infinite Prandtl number: Asymptotics and numerics, *Phys. Fluids* **25**, 113602 (2013).
- [53] S. Grossmann and D. Lohse, Thermal convection for large Prandtl numbers, *Phys. Rev. Lett.* **86**, 3316 (2001).
- [54] J. Jimenez and J. A. Zufria, A boundary-layer analysis of Rayleigh-bénard convection at large Rayleigh number, *J. Fluid Mech.* **178**, 53 (1987).
- [55] A. Maali, R. Boisgard, H. Chraïbi, Z. Zhang, H. Kellay, and A. Würger, Viscoelastic drag forces and crossover from no-slip to slip boundary conditions for flow near air-water interfaces, *Phys. Rev. Lett.* **118**, 084501 (2017).
- [56] L. N. Howard, Convection at high Rayleigh number, in *Applied Mechanics*, edited by H. Görtler (Springer Berlin Heidelberg, Berlin, Heidelberg, 1966) pp. 1109–1115.
- [57] M. V. R. Malkus, The heat transport and spectrum of thermal turbulence, *Proc. R. Soc. London A* **225**, 196 (1954).
- [58] Y. Song, M. Hao, Y. Liu, Y. Zhao, B. Su, and L. Jiang, CO₂ diffusion in n-hexadecane investigated using magnetic resonance imaging and pressure decay measurements, *RSC Advances* **4**, 50180 (2014).
- [59] P. Yang, H. Guo, Z. Wang, and Q. Zhou, Density and volumetric properties of binary mixtures of CO₂+ hexadecane from (303.2 to 473.2) K and pressures up to 50.0 MPa, *J. Chem. Eng. Data* **64**, 2568 (2019).
- [60] M. McBride-Wright, G. C. Maitland, and J. P. M. Trusler, Viscosity and density of aqueous solutions of carbon dioxide at temperatures from (274 to 449) K and at pressures up to 100 MPa, *J. Chem. Eng. Data* **60**, 171 (2015).
- [61] H. Watanabe and K. Izuka, The influence of dissolved gases on the density of water, *Metrologia* **21**, 19 (1985).
- [62] H. S. Carslaw and J. C. Jaeger, *Conduction of heat in solids*, Oxford: Clarendon Press (1959).
- [63] L. D. Landau and E. M. Lifshitz, Thermal conduction in fluids, in *Fluid Mechanics* (Pergamon, 1987) 2nd ed., Chap. 5, p. 200.
- [64] P. Peñas-López, M. A. Parrales, J. Rodríguez-Rodríguez, and D. van der Meer, The history effect in bubble growth and dissolution. Part 1. Theory, *J. Fluid Mech.* **800**, 180 (2016).
- [65] S. Chu and A. Prosperetti, Dissolution and growth of a multicomponent drop in an immiscible liquid, *J. Fluid Mech.* **798**, 787 (2016).
- [66] J. Crank, *The mathematics of diffusion*, 2nd ed. (Oxford University Press, 1975) pp. 49–52.